Cell Stem Cell

Article

Expansion of the neocortex and protection from neurodegeneration by *in vivo* transient reprogramming

Graphical abstract

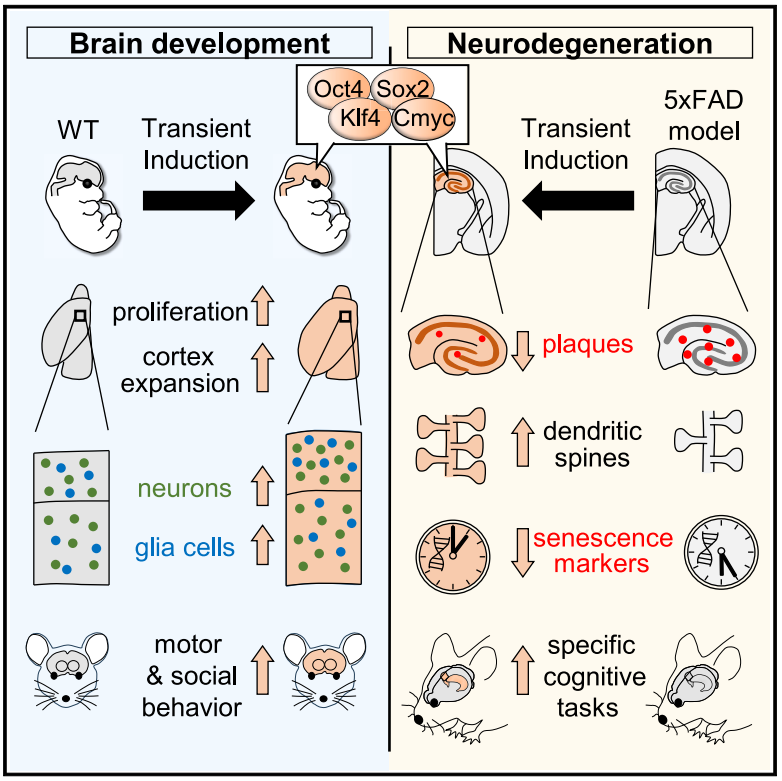

Authors

Yi-Ru Shen, Sofia Zaballa, Xavier Bech, ..., Rüdiger Klein, Albert Giralt, Daniel del Toro

Correspondence

ruediger.klein@bi.mpg.de (R.K.), albertgiralt@ub.edu (A.G.), danieldeltoro@ub.edu (D.d.T.)

In brief

Shen and Zaballa et al. report on using Yamanaka factors (YFs) for partial reprogramming in the mouse brain. During development, YF induction results in cortical expansion and improved behavior. Similar induction at adult stages prevents the development of several Alzheimer's disease hallmarks. These findings reveal YFs as a tool to increase neural proliferation and their potential use in brain disorders.

Highlights

- Transient Yamanaka factor (YF) expression during development expands neocortex
- YF-treated mice show enhanced cognitive skills
- Intermittent YF expression is tolerated by adult principal hippocampal neurons
- Long-term intermittent YF reprogramming is protective in an AD mouse model

Shen et al., 2024, Cell Stem Cell *31*, 1741–1759
December 5, 2024
https://doi.org/10.1016/j.stem.2024.09.013

CellPress

Cell Stem Cell

CellPress
OPEN ACCESS

Article

Expansion of the neocortex and protection from neurodegeneration by *in vivo* transient reprogramming

Yi-Ru Shen,[1,13] Sofia Zaballa,[2,3,13] Xavier Bech,[2,3] Anna Sancho-Balsells,[2,3] Irene Rodríguez-Navarro,[2,3] Carmen Cifuentes-Díaz,[4] Gönül Seyit-Bremer,[1] Seung Hee Chun,[1] Tobias Straub,[5] Jordi Abante,[2,6,7,8] Iñaki Merino-Valverde,[9] Laia Richart,[9] Vipul Gupta,[9] Hao-Yi Li,[1,10] Ivan Ballasch,[2,3] Noelia Alcázar,[11,12] Jordi Alberch,[2,3,7] Josep M. Canals,[2,6,7] Maria Abad,[9,11] Manuel Serrano,[9,12] Rüdiger Klein,[1,*] Albert Giralt,[2,3,7,*] and Daniel del Toro[2,3,7,14,*]

[1]Department of Molecules-Signaling-Development, Max-Planck Institute for Biological Intelligence, 82152 Martinsried, Germany
[2]Department of Biomedical Sciences, Faculty of Medicine and Health Sciences, Institute of Neurosciences, IDIBAPS, University of Barcelona, 08036 Barcelona, Spain
[3]CIBERNED, 08036 Barcelona, Spain
[4]Inserm UMR-S 1270, Sorbonne Université, Science and Engineering Faculty, and Institut du Fer a Moulin, 75005 Paris, France
[5]Bioinformatics Core, Biomedical Center, Faculty of Medicine, Lugwig-Maximilians University (LMU), 82152 Martinsried, Germany
[6]Laboratory of Stem Cells and Regenerative Medicine, University of Barcelona, 08036 Barcelona, Spain
[7]Creatio, Production and Validation Center of Advanced Therapies, Faculty of Medicine and Health Sciences, University of Barcelona, 08036 Barcelona, Spain
[8]Department of Mathematics & Computer Science, University of Barcelona, Barcelona, Spain
[9]Cambridge Institute of Science, Altos Labs, Granta Park, Cambridge CB21 6GP, UK
[10]Institute of Precision Medicine, College of Medicine, National Sun Yat-Sen University, Kaohsiung, Taiwan
[11]Vall d'Hebron Institute of Oncology (VHIO), 08035 Barcelona, Spain
[12]Institute for Research in Biomedicine (IRB Barcelona), Barcelona Institute of Science and Technology (BIST), Barcelona 08028, Spain
[13]These authors contributed equally
[14]Lead contact
*Correspondence: ruediger.klein@bi.mpg.de (R.K.), albertgiralt@ub.edu (A.G.), danieldeltoro@ub.edu (D.d.T.)
https://doi.org/10.1016/j.stem.2024.09.013

SUMMARY

Yamanaka factors (YFs) can reverse some aging features in mammalian tissues, but their effects on the brain remain largely unexplored. Here, we induced YFs in the mouse brain in a controlled spatiotemporal manner in two different scenarios: brain development and adult stages in the context of neurodegeneration. Embryonic induction of YFs perturbed cell identity of both progenitors and neurons, but transient and low-level expression is tolerated by these cells. Under these conditions, YF induction led to progenitor expansion, an increased number of upper cortical neurons and glia, and enhanced motor and social behavior in adult mice. Additionally, controlled YF induction is tolerated by principal neurons in the adult dorsal hippocampus and prevented the development of several hallmarks of Alzheimer's disease, including cognitive decline and altered molecular signatures, in the 5xFAD mouse model. These results highlight the powerful impact of YFs on neural proliferation and their potential use in brain disorders.

INTRODUCTION

The Yamanaka factors (YFs), a quartet of transcription factors—Oct4, Sox2, Klf4, and c-Myc—(OSKM, hereafter referred to as YFs), play a pivotal role in cellular biology due to their unparalleled ability to reprogram somatic cells to a pluripotent state.[1] This discovery has opened new research avenues, revealing their potential in tissue rejuvenation,[2,3] reversal of epigenetic modifications, and markers of cell damage,[4–6] thus ameliorating phenotypes associated with cellular aging.[2,7,8] Indeed, YFs have been employed to reverse age-associated hallmarks in various peripheral tissues, resulting in improved regeneration of muscle, optic nerve, cardiomyocytes, skin, and liver.[5,9–13] However, our understanding of their role, and the broader implications for the nervous system, is still in its nascent stages.

Ectopic YF expression can induce de-differentiation and pluripotency of somatic cells, erasing their epigenetic state and cellular identity.[6,14] This process has been linked to induced pluripotent cell (iPSC) formation mechanisms.[15,16] Continuous expression of these factors in mice often leads to tumoral masses and mortality within weeks.[17] Seminal work has confirmed that it is possible to safely express YFs *in vivo* through partial activation.[2,9] Intermittent activation in peripheral tissues preserves cell identity and enhances regeneration without

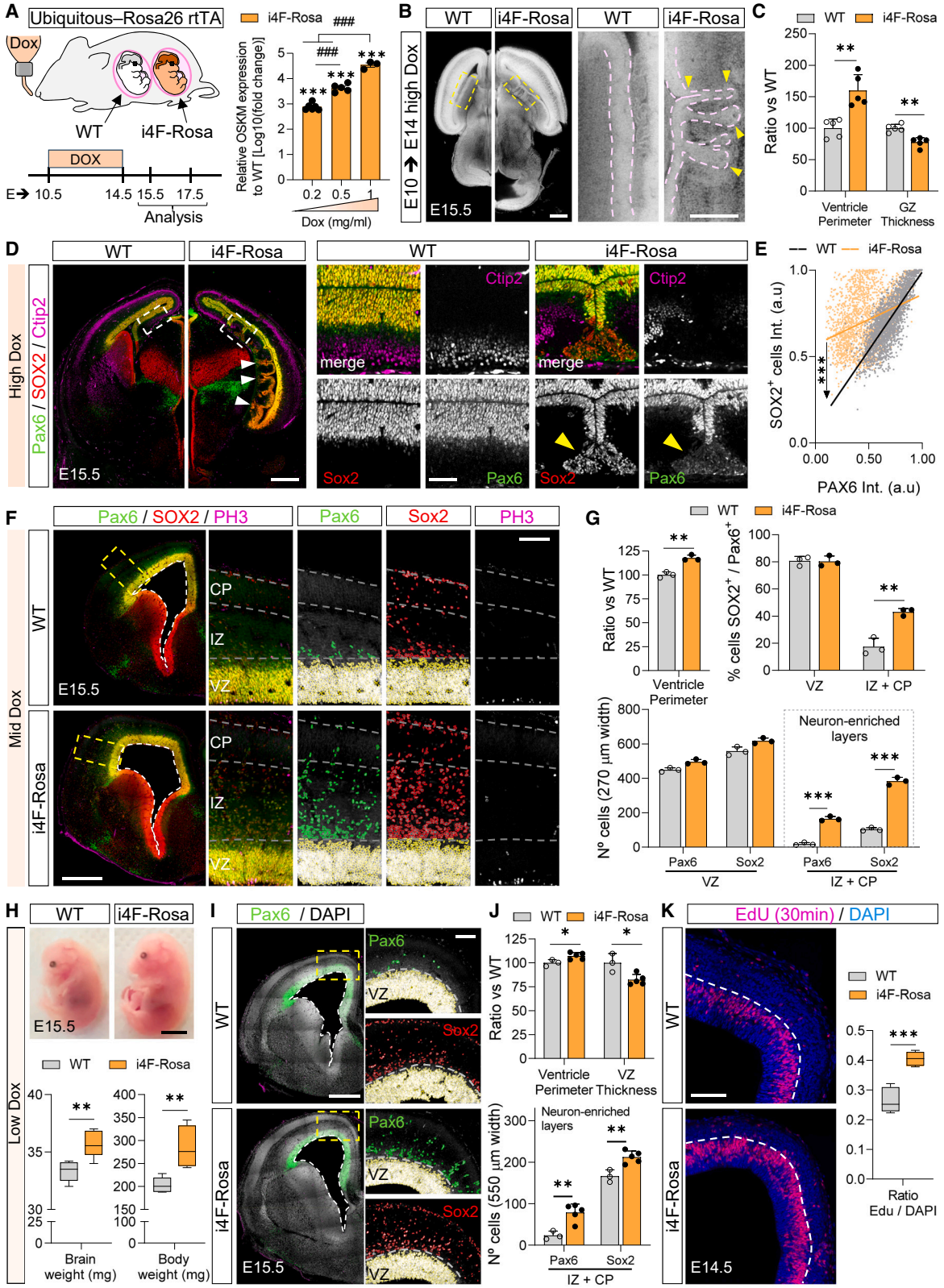

(legend on next page)

causing cancer.[2,4] Moreover, transient YF activation has been shown to increase proliferation via distinct mechanisms: (1) remodeling the stem cell niche in muscles[11] and (2) inducing transient de-differentiation of cardiomyocites.[12,13] Our knowledge remains scarce regarding the impact of transient YF induction on proliferation and/or rejuvenation in the nervous system.

Aging stands as the primary risk factor for Alzheimer's disease (AD), a phenomenon not entirely accounted for by the amyloid hypothesis.[18] Notably, AD and most neurodegenerative disorders present signatures of "accelerated" aging, including increased oxidation, diminished synaptic plasticity, and reduced metabolism.[19–21] In such scenarios, neurons progressively lose their regenerative capacity, attributed to transcriptomic and chromatin landscape alterations.[22] From a translational standpoint, YFs have facilitated cell replacement therapies for neurodegenerative diseases.[23] For instance, in Parkinson's disease, the transplantation of dopaminergic neurons derived from YF-induced iPSCs[24] yielded some motor improvements but also led to teratoma growth in immunodeficient mice.[25] Although most reprogramming strategies aim to generate neurons to replace damaged ones, two recent studies indicate that YFs can induce epigenetic modifications in neurons and promote axon regeneration post injury.[5,26] However, the application of YFs in mature neurons within the context of neurodegeneration remains unexplored.

Here, we employed a controlled spatiotemporal induction of YFs in the mouse brain across two distinct scenarios: during brain development and in adult stages within the context of neurodegeneration. Our focus on the impact of YFs on neurogenesis during development was influenced by recent findings that a subset of these factors is expressed in various neural progenitors early in this phase.[27] Here, we report that transient, low-level expression of YFs increased proliferation, resulting in an augmented output of neurons and glia, which led to an enlarged neocortex. This expansion was functionally reflected in enhanced motor and social behavior in adult mice. Because this induction protocol enhanced cognitive skills, we hypothesized that it could exert a similar effect in the context of a neurodegenerative disorder. Thus, we expressed YFs only in mature hippocampal neurons, using the 5xFAD mouse model of AD. We show that these neurons tolerate intermittent YF expression while preserving their identity. This safe approach led to cognitive, molecular, and histological improvements in the 5xFAD mice. Our results establish transient YF induction as a powerful tool for modulating neural proliferation, and it may open new therapeutic strategies for brain disorders.

RESULTS

Transient YF induction perturbs cell identity and increases proliferation

To study the effects of YF induction during development, we used the conditional inducible-four factors (i4F) mouse line that allows YF induction in a Tet-ON system.[17] We established an *in vivo* transient reprogramming protocol for systemic expression of YFs by using mice carrying a single copy of the i4F polycistronic cassette and a reverse tetracycline transactivator (rtTA) within the *Rosa26* locus (i4F-Rosa)[17] (Figure 1A). We induced YFs by administering doxycycline (Dox) in the drinking water of pregnant females for 4 days (embryonic day [E]10.5–E14.5), at three concentrations: high (1 mg/mL), medium (0.5 mg/mL), and low (0.2 mg/mL). Reverse transcription followed by quantitative PCR (RT-qPCR) confirmed Dox-dependent expression of the polycistronic OSKM messenger RNA (mRNA) (Figure 1A). Initial treatments of i4F-Rosa embryos and their littermate controls (wild type [WT]) with high Dox for 4 days led to bigger brains (Video S1) and a dramatic elongation of the germinal layer at E15.5. The total area of this layer expanded in proportion to the cortical area (Figures S1A and S1B), but was thinner in regions with invaginations of the ventricular surface (Figures 1B, 1C, and S1A; Video S1).

Immunostaining for Pax6 (found in apical progenitors [APs]) and Sox2 (expressed in neural progenitors and one of the YFs), showed expansion in the number of APs (Figures 1D and S1C). Despite their abundance, Pax6 intensity at the single-cell level was reduced (Figure 1E), suggesting that strong YF induction can perturb cell identity, as found in other systems.[17,28] This is evidenced by the loss of identity markers like Pax6 for progenitors and Ctip2 for neurons, along with the emergence of Nanog expression (Figures S1D–S1F). Given that the survival of i4F-Rosa embryos was compromised due to impaired liver hematopoiesis (data not shown), we reduced Dox concentration during the 4-day induction period.

Figure 1. Transient YF induction perturbs cell identity and increases proliferation

(A) Scheme of Dox treatment in wild-type (WT) and i4F-Rosa littermate embryos. Right graph shows RT-qPCR for OSKM mRNA of E15.5 i4F-Rosa embryos treated with different Dox concentrations from E10.5 to E14.5, normalized to control (3–6 embryos group). ***$p < 0.001$, Student's t test vs. WT samples. ###$p < 0.001$ one-way ANOVA.

(B) Sagittal sections of cleared whole-mount brains (E15.5) stained with propidium iodine after high Dox treatment (from E10.5 to E14.5). Higher magnification of dashed rectangles shown on the right. Pink dashed lines indicate the germinal zone, yellow arrowheads mark invaginations.

(C) Quantification from (B). $n = 5$ mice/group. **$p < 0.01$, Student's t test.

(D) E15.5 coronal brain sections, after 4 days high Dox, stained for neuronal progenitors (Pax6, green and Sox2, red) and neurons (Ctip2, magenta). Areas within dashed rectangles are enlarged on the right.

(E) Scatterplot quantification of Pax6 intensity in Sox2+ cells. $n = 2,339$ (WT) and 2,031 (i4F-Rosa) cells from 3–4 brains/group. ***$p < 0.001$, linear regression, Student's t test.

(F) Similar to (D), but E15.5 sections treated with 4 days Mid Dox, including mitotic marker (PH3, magenta).

(G) Quantification from (F). $n = 3$ mice/group. **$p < 0.01$, ***$p < 0.001$, Student's t test.

(H) E15.5 embryos after 4 days low Dox treatment. Brain and body weight is shown below. $n = 5–6$ mice/group. **$p < 0.01$, Student's t test.

(I) Similar to (F), except for sections treated with 4 days low Dox. Yellow dashed rectangles are enlarged on the right. Ventricle perimeter marked with white dashed lines.

(J) Quantification from (I) $n = 3–5$ mice/group. *$p < 0.05$, **$p < 0.01$, Student's t test.

(K) E14.5 cortices labeled with a short pulse (30 min) of EdU (red) and DAPI (blue, nuclei). Total EdU+ cells quantified on the right. $n = 6$ mice/group. ***$p < 0.001$, Student's t test. Scale bars, 500 μm (B, D, F, and I), 250 μm inset (B), 100 μm inset (D, F, I, and K), and 3 mm (H).

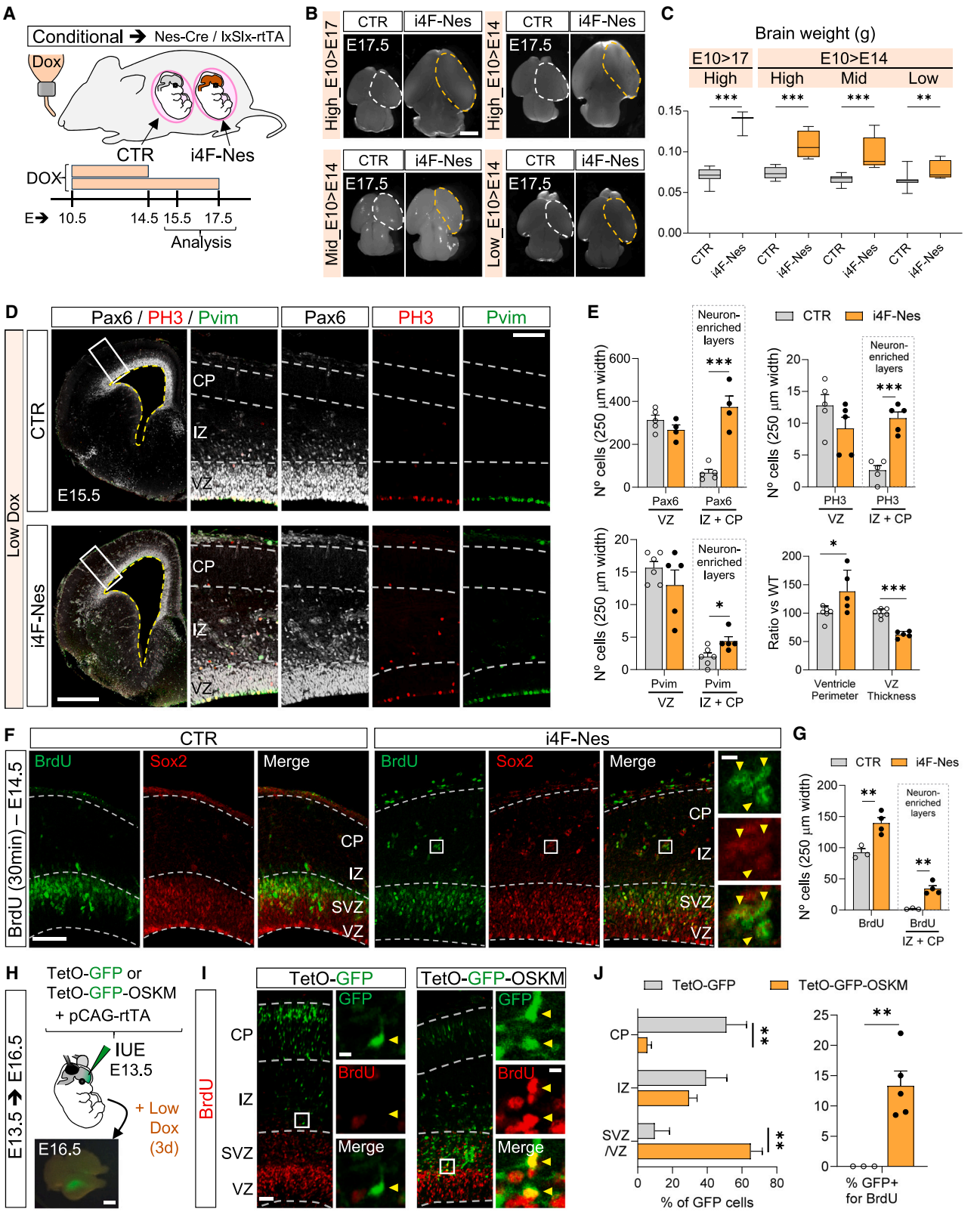

(legend on next page)

Medium YF induction also resulted in an enlarged ventricular zone (VZ) proportional to the increased brain weight (Figure S1G) but without invaginations and loss of Pax6 in APs (Figure 1F). Notably, the abundance of individual and double-positive Pax6+ and Sox2+ progenitors was significantly higher in neuron-enriched layers (intermediate zone [IZ] and cortical plate [CP]) (Figure 1G). Similar to high Dox treatment, very few i4F-Rosa embryos reached E17.5 stages due to altered hematopoiesis.

Next, i4F-Rosa embryos received low Dox treatment from E10.5 to E14.5, resulting in viable embryos with increased brain and body weight (Figures 1H and S1H). Histological analysis showed increased perimeter of the ventricles and a thinner germinal zone (Figures 1I and 1J). Pax6 expression was preserved in APs and there was an increase of Pax6+ and Sox2+ progenitors in neuronally enriched layers (IZ + CP) (Figures 1J and S1I), where we found Sox2+ cells co-expressing neuronal markers like Ctip2 (Figures S1J and S1K). Similar to medium YF induction, no change was observed in the density of cells stained for phosphorylated vimentin (Pvim) and histone H3 (PH3), which label dividing radial glial (RG) and mitotic cells, respectively, at E15.5 (Figures S1L and S1M). Short pulses of EdU revealed increased cell proliferation in the germinal zone (Figure 1K). We next asked whether this proliferation impacted the migration and distribution of pyramidal neurons. Cortical layering was preserved (data not shown) and the proportion of newborn neurons, identified by EdU pulse labeling, was normal in the CP at E15.5 (Figures S1N and S1O). These results indicate that YF induction can perturb cell identity and increase proliferation during development.

Nervous-system-specific induction of YFs leads to cortical expansion

To remove any detrimental effects of ubiquitous YF induction during development, i4F mice were crossed with Cre-dependent floxed rtTA and the nervous-system-specific Nestin-Cre line. This mouse model (i4F-Nes) allows the study of high and longer Dox treatments (Figure 2A). We found that high Dox or longer treatments resulted in much bigger brains, with an expanded cortex and a weight up to double that of control littermates (CTR) at E17.5 (Figures 2B, 2C, and S2A). Moreover, we observed strong induction of YFs like c-Myc, Oct4, and Sox2, together with Nanog, in germinal and neuronal layers after high Dox treatment (Figures S2B and S2C). Upon further inspection of i4F-Nes embryos treated with different conditions, we focused on the low Dox treatment (4 days, E10.5–E14.5) because it preserved brain morphology and survival to adult stages, as in the i4F-Rosa line. We found increased numbers of basal PH3+ and Pvim+ cells in i4F-Nes embryos at E15.5 (Figures 2D and 2E). The number of Pax6+ progenitors also increased (Figure S2D), mainly from their presence in neuron-enriched layers (IZ + CP) (Figure 2E). A short pulse of bromodeoxyuridine (BrdU) revealed increased proliferation, with fewer Sox2+ cells labeled in the IZ (Figures 2F and 2G). These results, including increased lateral ventricle perimeter and reduced VZ thickness (Figure 2E), were similar to those found in the i4F-Rosa line with the same treatment. This suggests that the observed changes in i4F-Rosa brains largely result from YF induction effects in the nervous system.

We next asked whether the few Sox2+ and BrdU+ cells in the IZ (Figures 2F and 2G) resulted from ectopic migration of APs or expression of YFs. Using *in utero* electroporation at E13.5, we expressed YFs and GFP (TeTO-OSKM-GFP), or GFP as a control (TetO-GFP), in a Tet-ON system with low Dox for 3 days (Figure 2H). Most OSKM-expressing cells remained in the germinal zone and were proliferative (Figures 2I and 2J), expressing YFs like Sox2 and Oct4 (Figures S2E and S2F). These results suggest that the transient abnormal localization of Sox2 and Pax6 in neuron-enriched layers is due to ectopic expression, not premature migration. Proteomic profiling revealed increased YF proteins like Sox2 and Klf4, changes in extracellular matrix (ECM) components, and reduced cell adhesion proteins like Cdh8 and Neo1 in i4F-Nes cortices (Figures S2G and S2H), linked to increased cell proliferation.[29,30] Overall, these results indicate that conditional nervous-system YF induction transiently perturbs cell behavior, increasing progenitors and proliferation.

YF-induction effects on single-cell transcriptomics

We investigated YF-induction effects on transcriptomic profiles and cell composition by single-cell RNA sequencing (scRNA-seq) on E15.5 CTR and i4F-Nes embryo cortices after 4 days low Dox treatment (Figure 3A). We obtained 12.196 (CTR) and 12.757 (i4F-Nes) single-cell transcriptomes, averaging 4,027 genes per cell (Figure S3A), and performed principal-component analysis (PCA), uniform manifold approximation and projection (UMAP) dimensionality reduction, and unsupervised clustering. We assigned cell clusters into cell classes based on the coexpression of multiple marker genes, as done in previous studies[31] (Figures S3B–S3E). As expected, we found the major clusters related to cortical development: neurons, intermediate progenitors (IPs) and APs, and other less abundant cell classes such as interneurons (INs), microglia, Cajal Retzius (CR), and endothelial cells (ECs) (Figure 3B).

Figure 2. Nervous-system-specific YF induction leads to cortical expansion

(A) Scheme of Dox treatment in control (CTR) and i4F-Nes embryos.

(B) Top view of E17.5 brains from CTR and i4F-Nes embryos with different Dox treatments. Dashed lines delineate one hemisphere's cortical area.

(C) Brain weight from (B). $n = 5–6$ mice/group. $^{**}p < 0.01$, $^{***}p > 0.001$, Student's t test.

(D) E15.5 coronal brain sections, after low Dox (E10.5–E14.5), stained for Pax6 (white), Pvim (green), and PH3 (red). Magnified dashed rectangles on the right.

(E) Data quantification from (D). $n = 4–6$ mice/group. $^{*}p < 0.05$, $^{***}p < 0.001$, Student's t test.

(F) E14.5 cortices after a 30-min BrdU pulse (green) and Sox2 staining (red). Magnified white rectangles on the right.

(G) Data quantification from (F). $n = 3$ mice/group. $^{**}p < 0.01$, Student's t test.

(H) WT embryos electroporated at E13.5 to express YF and GFP via Tet-ON system, treated with 3 days Dox, and labeled with a 12 h BrdU pulse (red).

(I) Distribution of GFP+ cells and insets showing OSKM-expressing cells positive for BrdU on the right.

(J) Quantification from (I). $n = 3–5$ mice/group. $^{**}p < 0.01$, Student's t test. Scale bars, 1 mm (B and H), 500 μm (D), 100 μm (F and I), 100 μm inset (D), and 12 μm (F and I).

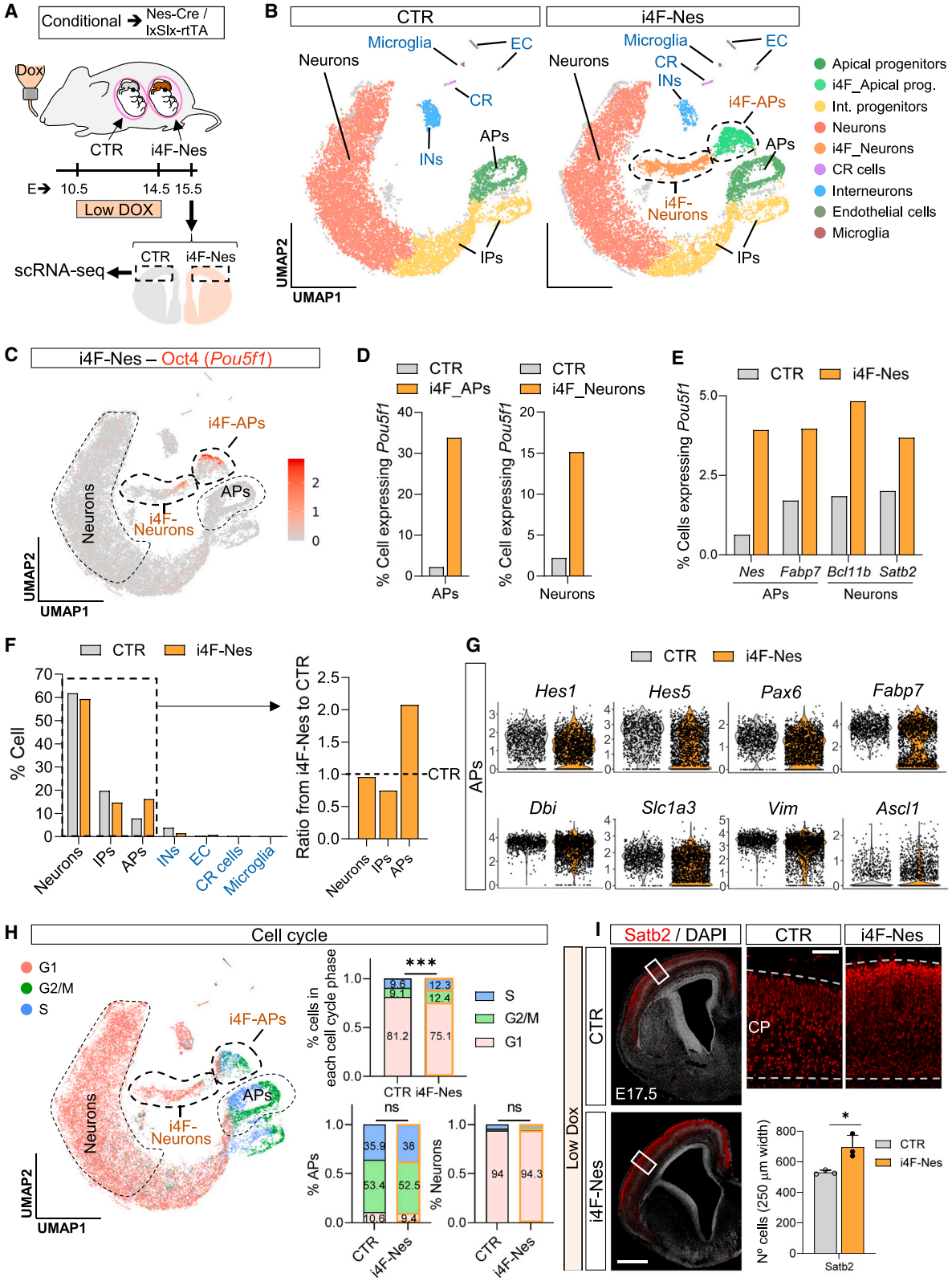

(legend on next page)

The cellular composition of most clusters was consistent between CTR and i4F-Nes conditions, except for two novel populations in the i4F-Nes condition: a neuron-like (i4F-Neurons) and AP-like (i4F-APs) cluster (Figure 3B). These new populations had a significant increase in the expression of one of the YFs, Oct4 (*Pou5f1*), with levels reaching 30% in i4F-APs and 15% in i4F-Neurons (Figures 3C and 3D). Elevated Oct4 was also observed in total APs (*Nes* and *Fabp7*) and neuron populations (*Bcl11b* and *Satb2*) in the i4F-Nes condition (Figure 3E). We identified differentially expressed genes (DEGs) between i4F-Neuron, i4F-AP, and their control groups (Tables S1 and S2). Analysis of the 20 most enriched biological processes, predicted using fold enrichment with the ShinyGO tool,[32] revealed that these new populations are less mature (Figure S3F). When analyzing cell distribution, APs showed the most significant difference, with a 2-fold increase in i4F-Nes vs. CTR (Figure 3F), consistent with the increased number of cells expressing apical and radial glia progenitors genes (Figure 3G). We next calculated the fraction of cells assigned to the different cell-cycle phases (G1, G2/M, and S) by the expression of representative genes.[33] We observed more cells in the S and G2/M phases and fewer in the G1 phase in the i4F-Nes condition (Figure 3H). This change is due to the overall abundance of APs in this condition (Figure 3E), as cell-cycle distributions between APs and neurons from CTR and i4F-Nes conditions were similar (Figure 3H). The expansion of neuronal progenitors resulted in an increased number of upper cortical neurons at E17.5 (Figure 3I). These results suggest that YF induction expands progenitor numbers and enhances proliferation.

Improved behavioral performance after YF induction

The cortical expansion in both i4F-Rosa and i4F-Nes mouse lines persisted into adulthood, with adult (5-month-old) mice showing increased neuron numbers and enlarged layer II–IV (Figures 4A and 4B). Given that RG cells are the source of both cortical neurons and glia,[34] we asked whether glial cells could contribute to the enlarged cortex. Both lines showed an increased number of astrocytes (GFAP+) and other glial cells like microglia (Iba1+) and oligodendrocytes (MBP+) (Figures 4C, 4D, and S4A–S4G). Similar to neurons, the largest increases in glial cells occurred in the prefrontal and motor cortical areas (Figures S4A–S4G; data not shown). Increases in astrocytes were detectable by post-natal day 4 (P4) (Figures S4C–S4E). No changes in apoptosis were observed at P4 or in adulthood (Figures S4H and S4I). Given that both neurons and glia increased in similar proportions, their ratio was preserved.

Higher cognitive abilities are thought to arise from cortical expansion during evolution.[35,36] We thus tested whether cortical expansion by YF induction could affect specific behaviors. We subjected 5-month-old i4F-Rosa and i4F-Nes mice, with their respective controls (WT and CTR, respectively), to a battery of behavioral tests. The open field test showed no significant differences in the exploration between i4F-Rosa, i4F-Nes, and their controls (Figure 4E). In the elevated-plus maze, no significant differences were observed in the time spent in open and closed arms between i4F-Rosa and WT mice. Notably, i4F-Nes mice showed an increased time exploring the open arms (Figure 4F). This indicates that transient induction of YFs during development has no effect (i4F-Rosa) or even reduces (i4F-Nes) anxiety-like behavior in adults (Figure 4F). We assessed higher-order cognitive functions related to cortical functions like motor learning, compulsive-like behavior, and sociability.[37,38] In the accelerating rotarod test for motor learning,[39] i4F-Rosa mice showed an enhanced ability to maintain their balance compared with WT mice (Figure 4G). The average of the last two sessions, where a learning plateau was reached, was used to compare their motor performance. Both i4F-Rosa and i4F-Nes mice exhibited improved motor performance compared with their controls (Figure 4G). Then, we performed the marble burying test to evaluate compulsive-like behaviors.[40] i4F-Rosa mice buried fewer marbles than WT (Figure 4H), indicating reduced compulsive behavior. To evaluate sociability, we performed the three-chamber social interaction test.[41] In this paradigm, both i4F-Rosa and i4F-Nes mice showed an increased sociability index when compared with their respective controls (Figures 4I and 4J). We conclude that cortical expansion by transient YF induction during development improves motor and social behavior of adult mice.

Intermittent YF induction in adult hippocampal neurons is tolerated and prevents synaptic loss in the 5xFAD mouse model

YFs have been shown to reverse some aging features in mammalian tissues.[2,5,9,10] Given that transient YF induction is tolerated by post-mitotic neurons during development and enhances cognitive skills, we hypothesized that a similar protocol in adult stages might protect against neurodegeneration. First, we established an *in vivo* intermittent YF induction protocol using a similar Dox treatment tolerated during development. YF induction was driven by synapsin-1 (SYN1)-dependent rtTA-expressing adeno-associated virus (AAV) injected into the dorsal hippocampus of 8-week-old i4F mice (Figure 5A). RT-qPCR confirmed Dox-dependent OSKM mRNA expression following low (0.2 mg/mL) and high (3 mg/mL) Dox treatments (Figure 5B). We introduced a ZsGreen reporter driven by a tetracycline

Figure 3. scRNA-seq analysis of control and i4F-Nes cortical populations

(A) Scheme of Dox treatment in CTR and i4F-Nes embryos, and collected area for scRNA-seq analysis.

(B) UMAP with cells colored by type. i4F_Apical prog., i4F-specific apical progenitors; Int. progenitors, intermediate progenitors; CR cells, Cajal Retzius cells.

(C) UMAP visualization with expression of one of the Yamanaka factors, *Pou5f1* (Oct4).

(D) Proportions of CTR and i4F-specific APs and i4F-specific neurons expressing *Pou5f1*.

(E) Proportions of APs (*Nes*, *Fabp7* [BLBP]) and neurons (*Bcl11b* [Ctip2], *Satb2*) expressing Pou5f1.

(F) Cell population proportions in CTR and i4F-Nes cortices.

(G) Violin plots levels of *Hes*, *Hes5*, *Pax6*, *Fabp7*, *Dbi*, *Slc1a3*, *Vim*, and *Ascl1* in both cortices.

(H) Cell-cycle analysis of CTR and i4F-Nes cells. UMAP visualization with cells colored by cell-cycle phase. Proportions of all cells, APs, and neurons in S, G2/M, and G1 phase on the right. $^{***}p < 0.001$ $\chi^2 = 119.57$, degree of freedom (df) = 2 between CTR and i4F-Nes proportions.

(I) E17.5 sections, after 4 days of low Dox, stained for Satb2 (red) and DAPI (white). Magnified dashed rectangles and quantification of neuron number on the right. $n = 3$ mice/group. $^{*}p < 0.05$, Student's t test. Scale bars, 500 μm (I) and 100 μm inset (I).

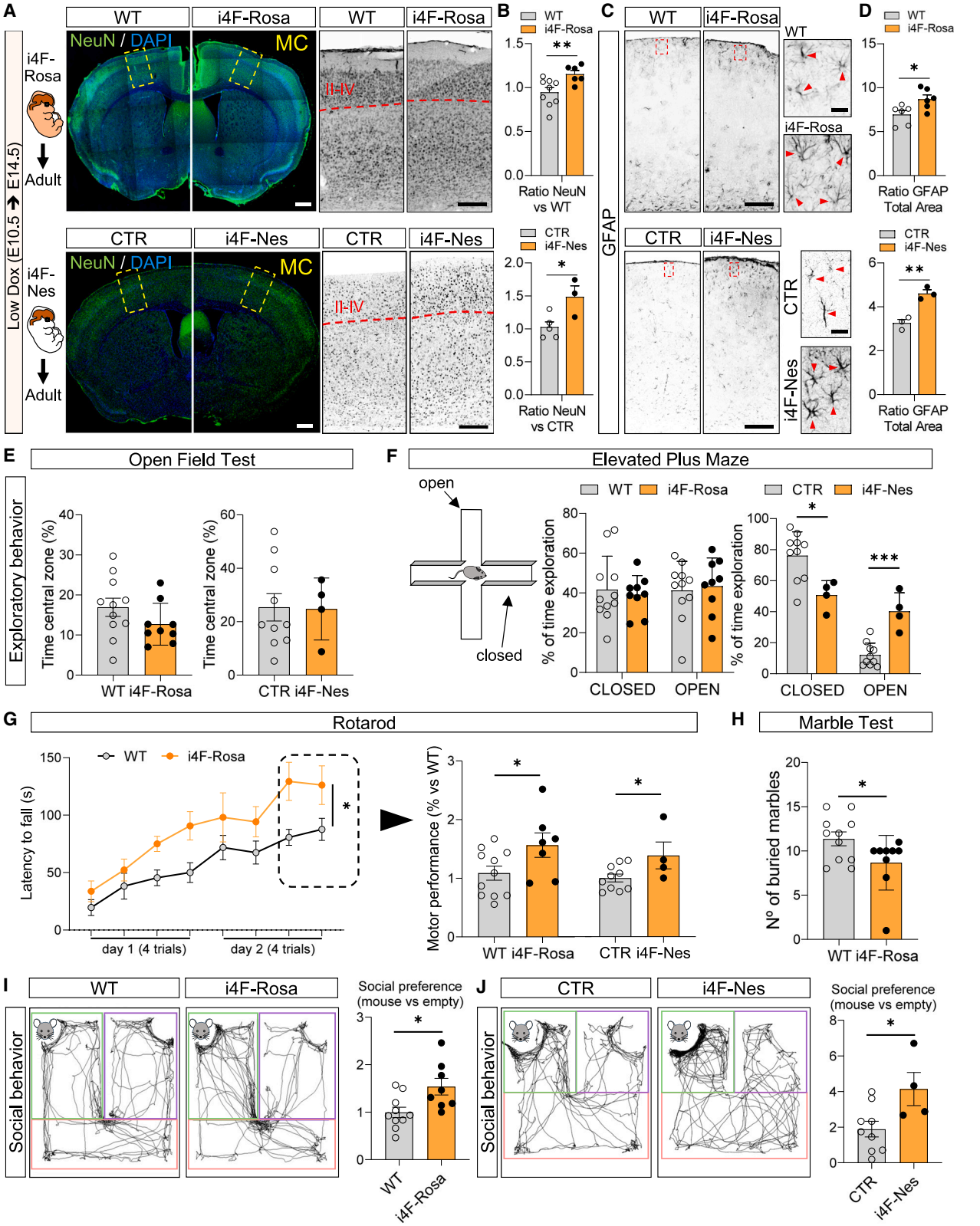

(legend on next page)

operator (TRE) promoter to visualize neurons expressing YFs after Dox treatment, which also demonstrated Dox-dependent activation (Figure 5C). We chose the low Dox dosage, because it was tolerated during development, and the 5xFAD mouse model, a robust model of AD.[42] 5xFAD mice were crossed with the i4F mouse line, generating the i4F/5xFAD mouse line and its littermate controls (i4F). From 12 to 35 weeks, both groups (i4F/5xFAD and its control i4F) were treated with vehicle (VEH) or low Dox (0.2 mg/mL), 3 days ON and 4 days OFF per week (Figure 5D). After treatment (8 months old), all groups were subjected to comprehensive behavioral, histological, and molecular experiments (Figure 5D).

Our intermittent YF induction was well tolerated, and survival was not affected in any experimental group (Figure 5E). No changes in body (data not shown) or brain weight were found at 8 months (Figure 5F). We assessed hippocampal anatomy and neuronal identity of the targeted cells. First, our intermittent YF induction did not affect the hippocampal organization and gross anatomy (Figure 5G). Targeted neurons with correct TRE promoter activation were found expressing ZsGreen in the Dox-treated groups (Figures 5G and 5H). Second, immunostaining for two mature neuron markers, NeuN and Pyk2, showed that YF induction did not alter the identity of transduced granule cells of the dentate gyrus (DG) (Figures 5I and S5A). Third, we confirmed that intermittent reprogramming does not, per se, alter the expression of the APP/PSEN1 transgene in the 5xFAD mouse model (Figure 5J).

We evaluated structural plasticity in granular neurons by Golgi staining on brain samples with complete transduction in the granular layer. We found the expected reduction in spine density of secondary dendrites in i4F/5xFAD treated with VEH (i4F/5xFAD-VEH) compared with the control i4F-VEH group (Figure 5K). Notably, this reduction was rescued in the Dox-treated i4F/5xFAD group (i4F/5xFAD-Dox) (Figure 5L). Next, we examined presynaptic and postsynaptic changes using electron microscopy. We quantified the numbers of presynaptic vesicles per synapse and the postsynaptic density (PSD) area in the DG molecular layer in all groups at 8 months (Figures 5M and S5B). Presynaptic vesicles per synapse were decreased in the i4F/5xFAD-VEH, as described previously,[43] but rescued in the i4F/5xFAD Dox group (Figure 5N). We additionally found that the PSD area was increased in both mouse groups (i4F and I4F/5xFAD) subjected to intermittent reprogramming (Figure 5N). These results revealed that intermittent YF induction is tolerated by adult hippocampal neurons and induced synaptic improvements in the 5xFAD mouse model.

Amelioration of AD-related hippocampal plaques and proteomic signatures by YF induction

Because 5xFAD mice develop severe amyloid pathology and proteomic changes in the hippocampus from 2 to 8 months of age,[42,44] we investigated the possible benefits of intermittent YF induction during this period. We quantified the plaque load in the CA1, CA3, and DG (Figure 6A) by Aβ immunolabeling. The number (Figure 6B) and size (Figures S5C and S5D) of plaques in these regions were strongly reduced in i4F/5xFAD Dox compared with i4F/5xFAD-VEH mice. Plaque numbers remained unchanged in regions without YF induction, such as the cortex (Figure 6B). We next conducted additional neuropathological studies. Microglial interaction with plaques was higher in i4F/5xFAD-Dox mice compared with i4F/5xFAD-VEH mice, correlating with smaller plaques and unchanged Iba1 expression (Figures S5E and S5F). Spectrin-dependent cleavage showed no differences between groups (Figure S6A). We examined astrogliosis: increased GFAP reactivity and total protein levels (Figure S6B) were not rescued in i4F/5xFAD-Dox mice, although morphological changes like astrocyte perimeter and area were normalized (Figures S6C–S6E). Finally, Tau phosphorylation at serine 396 was elevated in both i4F/5xFAD-Dox and i4F/5xFAD-VEH mice, with no differences between them (Figure S6F).

Next, we performed quantitative proteomic profiling of the DG (Figure 6C). This region is critical for learning and memory, and it is one of the most-affected hippocampal areas in AD.[45] Proteomics analysis showed that the transgene expression of *APP* present in the 5xFAD mouse was not affected by YF induction at 8 months (Figure 6D), consistent with RT-qPCR experiments (Figure 5J). Other AD-related markers,[44,46] such as β-amyloid clearance (APP,ApoE), neuroinflammation (GFAP,ABCA1), and stress responses (c4b,Pld3) were unchanged in adult i4F/5xFAD-Dox compared with the i4F/5xFAD-VEH group (Figure 6D). Next, we identified 950 differentially expressed proteins (DEPs) between i4F/5xFAD-VEH and their controls, i4F-VEH. The 20 most enriched KEEG pathways were predicted using fold enrichment analysis with the ShinyGO tool[32] and visualized

Figure 4. Increased behavioral performance after transient YF induction

(A) Scheme of mice used for adult behavioral experiments (4–5 months old). i4F-Rosa and i4F-Nes mutant embryos and their controls (WT and CTR) treated for 4 days with low Dox during development. Adult coronal sections stained with the neuronal marker NeuN (green) and DAPI (blue). Magnified dashed rectangles on the right.

(B) Quantification from (A). n = 9–11 mice/group (i4F-Rosa), n = 3–5 mice/group (i4F-Nes). $^{*}p < 0.05$, $^{**}p < 0.01$, Student's t test.

(C) As in (A), but using GFAP staining.

(D) Quantification from (C). n = 6 mice/group (i4F-Rosa), n = 3–5 mice/group (i4F-Nes). $^{*}p < 0.05$, $^{**}p < 0.01$, Student's t test.

(E) Percentage of time in the central zone of i4F-Rosa (9), i4F-Nes (4), and their controls: WT (11) and CTR (10).

(F) Percentage of time in closed/open arms. n = 11 (WT), 9 (i4F-Rosa), 10 (CTR), and 4 (i4F-Nes). $^{*}p < 0.05$, $^{***}p < 0.001$, two-way ANOVA.

(G) Latency to fall in the accelerating rotarod task. n = 11 (WT) and 9 (i4F-Rosa). $^{*}p < 0.05$, two-way ANOVA. Average of last two sessions per mice on the right. n = 11 (WT), 9 (i4F-Rosa), 10 (CTR), and 4 (i4F-Nes). $^{*}p < 0.05$, Student's t test.

(H) Number of buried marbles during 20 min session. n = 11 (WT), 9 (i4F-Rosa), $^{*}p < 0.05$, Student's t test.

(I) Social preference index in the three-chamber social interaction test. Representative track paths and the target mouse location (green area), empty cage (magenta area), and connecting chamber (red area). Ratios based on time spent on the target mouse vs. empty cage. n = 11 (WT), 9 (i4F-Rosa), $^{*}p < 0.05$, Student's t test.

(J) As in (H), but for i4F-Nes and controls (CTR). n = 10 (CTR) and 4 (i4F-Nes). $^{*}p < 0.05$, Student's t test. Scale bars, 500 μm (A), 200 μm (C), 200 μm inset (A), and 50 μm inset (C).

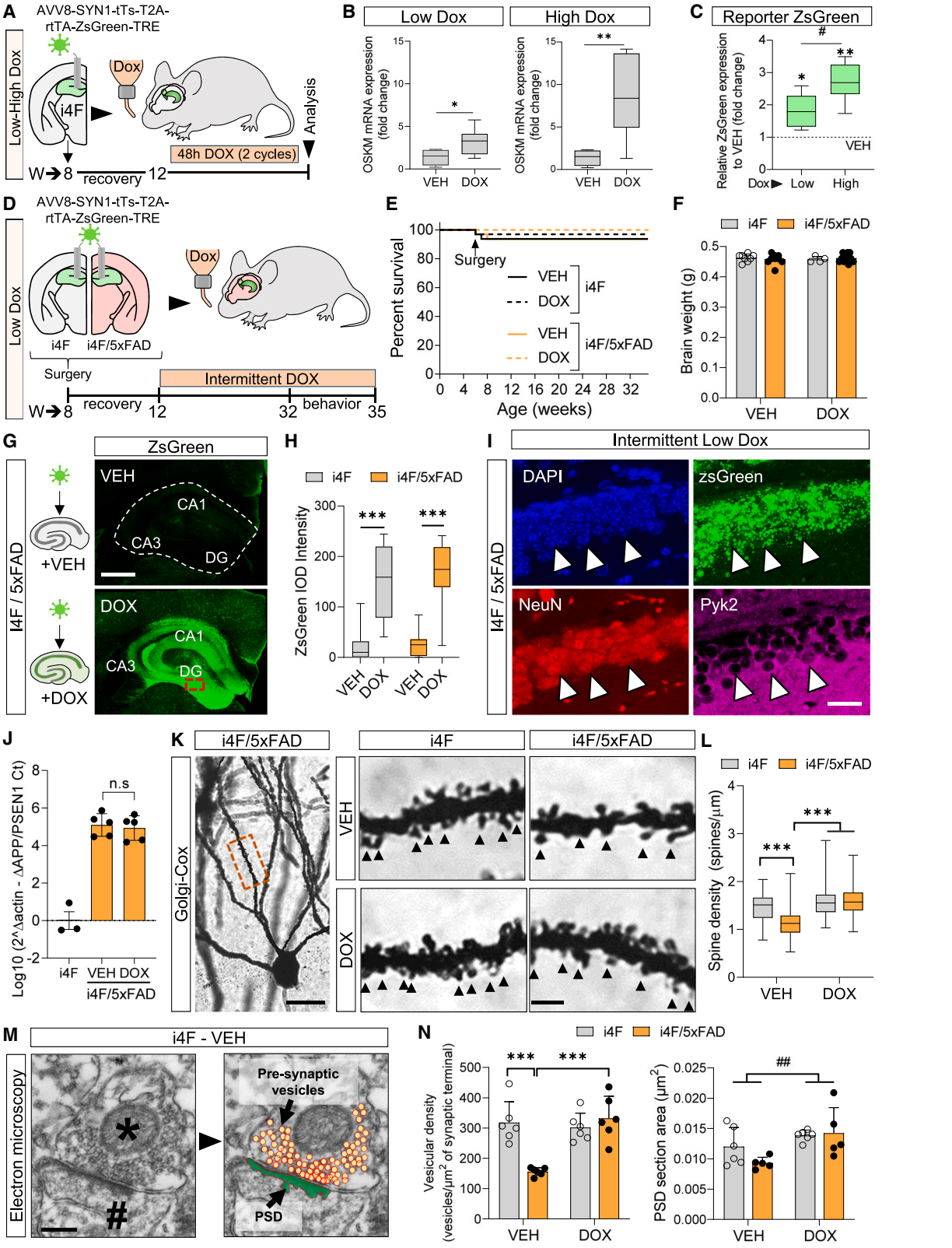

(legend on next page)

as an interaction network using Cytospace[47] (Figure 6E). These pathways were functionally related to neurodegenerative processes (Figure 6E), as described previously.[44] Enrichment analysis showed that 19 out of the 20 most significantly enriched pathways altered in i4F/5xFAD-VEH vs. i4F-VEH were partially rescued in the i4F/5xFAD-Dox group, suggesting that intermittent YF induction ameliorates proteomic changes in the 5xFAD mouse model (Figure 6F). Among 950 DEPs found in the i4F/5xFAD-VEH, 493 were normalized in the i4F/5xFAD-Dox compared with i4F-VEH control group. To explore the collective functions of the rescued DEPs, we constructed a network model focusing on 103 DEPs related to AD.[44] The results showed that the rescued pathways in i4F/5xFAD-Dox group were related to the pathogenesis of AD (mitochondria function, cellular metabolic processes, and cellular adhesion) (Figure 6G).

Given that intermittent YF induction ameliorated aging-related processes, we evaluated the epigenetic age of DG samples from i4F and VEH/Dox-treated i4F/5xFAD mice. The age was predicted using DNA methylation data obtained from the Horvath mammal 320K array.[48] Specifically, we used four clocks, trained on independent whole-brain datasets,[49] two of which consistently indicated age acceleration in i4F/5xFAD mice when compared with i4F (Table S3). In line with our *in vivo* observations, Dox treatment in i4F/5xFAD mice led to a significant or near-significant reduction in DNA-methylation-based epigenetic age (Figure 6H; Table S3). Additionally, cellular senescence markers Sirt1 and H3K9me3 increased in the DG of i4F/5xFAD-VEH, consistent with previous studies,[50] but were normalized in the i4F/5xFAD-Dox mice (Figures S6G–S6J). These findings suggest that intermittent YF induction rescues several AD-related hallmarks in the 5xFAD mouse model.

YF induction prevents cognitive decline in the 5xFAD mouse model

The recovery of several AD-related hallmarks of the 5xFAD mouse model with intermittent YF induction (i4F/5xFAD-Dox) prompted us to explore potential improvements in the cognitive deficits present at 8 months of age in hippocampus-related tasks.[42,51–53] We conducted several behavioral tests evaluating emotional and cognitive skills (Figure 7A). Results from the plus maze (Figure 7B) and forced swimming test (Figure 7C) revealed significant differences between i4F/5xFAD (VEH and Dox groups) and their respective controls (i4F-VEH and -Dox), but no changes between i4F/5xFAD treated with Dox or VEH. This suggest that although the 5xFAD genotype is associated with disturbances on anxiety or mood-related behaviors, they were not modified by YF induction in the dorsal hippocampus. This result agrees with studies linking emotional-like behaviors to the ventral hippocampus, whereas the dorsal region is principally involved with cognitive functions.[54]

Next, we applied different tasks to compare memory performance in these mice. We first evaluated cognitive flexibility and spatial memory in a T-maze (Figures 7D and 7E). We found that i4F/5xFAD-VEH mice alternated less than the i4F-VEH control group, indicating cognitive inflexibility. Notably, both the i4F-Dox and i4F/5xFAD-Dox groups performed better, i.e., more flexibly, than the i4F-VEH group (Figure 7D). We quantified the time mice spent exploring the familiar vs. the novel arm. i4F/5xFAD-VEH mice displayed no preference for the novel arm. This effect was rescued in the i4F/5xFAD-Dox group (Figure 7E). The novel object location test also showed that i4F/5xFAD-Dox had rescued the preference for novel objects that is lost in the i4F/5xFAD-VEH mice (Figure 7F). In the Y-maze, assessing spatial working memory,[55] i4F-VEH and i4F-Dox mice displayed a spontaneous alternation over the chance level (∼65%). The arm choice was decreased to ∼50% (chance levels) in the i4F/5xFAD-VEH mice but restored in the i4F/5xFAD-Dox mice (Figure 7G). Finally, we evaluated associative memory in the passive avoidance task. Latency to step-through was similar between groups during training (Figure 7H). In the test session, although all groups showed increased latency to enter the dark compartment 24 h after an electrical shock, this latency was shorter in i4F/5xFAD-VEH mice compared with the i4F-VEH control group and rescued in i4F/5xFAD-Dox mice (Figure 7H). Additional

Figure 5. *In vivo* YF induction in the 5xFAD mouse model

(A) Schematic and delivery of AAV-SYN1-tTs-T2A-rtTA-ZsGreen-TRE into i4F hippocampus.

(B) Hippocampal OSKM and mRNA levels following 0.2 (left) or 3 (right) mg/mL Dox treatment by RT-qPCR. n = 4–7 mice group. *$p < 0.05$, **$p < 0.01$, Student's t test.

(C) As in (B) but for ZsGreen mRNA levels. n = 4–7 mice group. #p < 0.05 (between High and Low) and*$p < 0.05$, **$p < 0.01$ relative to VEH, Student's t test.

(D) Design and AAV-SYN1-tTs-T2A-rtTA-ZsGreen-TRE delivery into the hippocampus of i4F and i4F/5xFAD mice, treated with intermittent Dox or vehicle (VEH) for 5 months.

(E) Survival outcome during experimental protocol (n = 15–20 mice/group).

(F) Total brain weight at the end of the protocol. n = 15–20 mice/group.

(G) Validation of rtTA-dependent ZsGreen signal after 5 months' Dox and VEH intermittent treatment. ZsGreen intensity (green) in coronal hippocampal sections of Dox- and VEH-treated i4F/5xFAD mice (8 months old). Red dashed rectangle is magnified on (I).

(H) ZsGreen intensity whisker plot. n = 15–20 mice/group. ***$p < 0.001$ Dox vs. VEH in each group, two-way ANOVA with Bonferroni's post hoc test.

(I) ZsGreen signal (green) stained with NeuN (red), Pyk2 (mature principal neuron, magenta), and DAPI (blue).

(J) RT-qPCR for APP/PSEN1 transgene in the hippocampus of i4F and i4F/5xFAD treated with VEH or Dox for 5 months, normalized to actin n = 3–5 mice/group. n.s. not significant.

(K) Golgi-Cox-stained granular neuron in the DG molecular layer. Orange dashed rectangle indicates the analyzed region of the secondary apical dendrite, magnified on the right. Black arrowheads indicate dendritic spines.

(L) Dendritic spine quantification. n = 7–11 mice/group (100–150 dendrites per group). ***$p < 0.001$, two-way ANOVA with Bonferroni's post hoc test.

(M) Electron microscope image of an excitatory synapse in the molecular layer of the DG in 8-month-old i4F-VEH. Asterisk indicates the presynaptic and hashtag the postsynaptic component. Presynaptic vesicles colored with orange circles; postsynaptic density (PSD) in green.

(N) Vesicular density and PSD area quantification. n = 6 mice/group. ## $p < 0.01$, **$p < 0.01$, ***$p < 0.001$, two-way ANOVA with Bonferroni's post hoc test. The left panel shows post hoc pairwise group comparisons, marked by asterisks, whereas the right panel uses hashtags to indicate differences in global treatment effects. Scale bars, 400 μm (G), 100 μm (I), 15, 3 μm (inset) (K), and 0.25 μm (M).

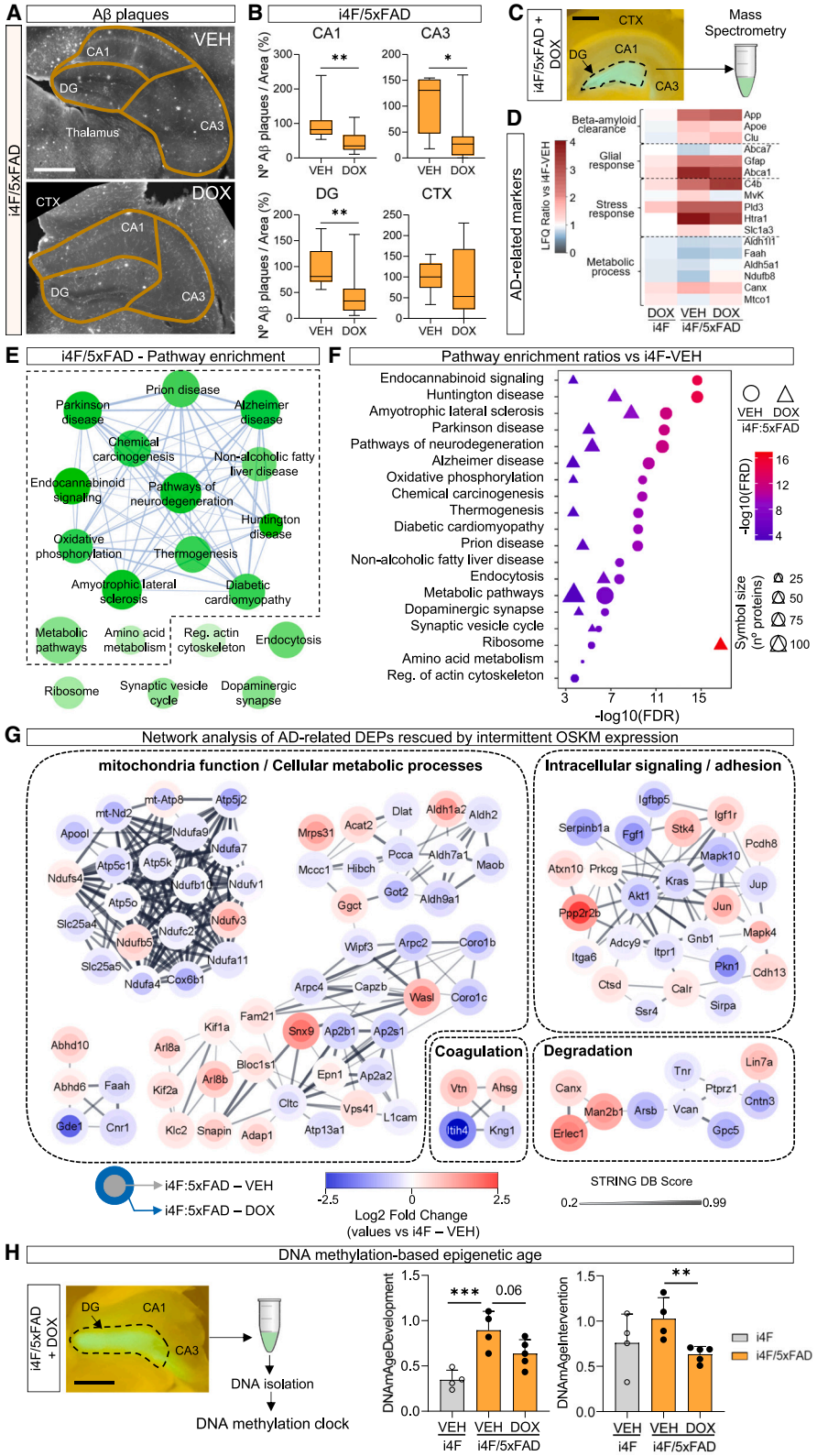

(legend on next page)

controls testing the effects of Dox treatment alone showed no differences in either WT or 5xFAD mice (Figure S7). Overall, YF induction in the dorsal hippocampus of the 5xFAD mice ameliorated some of the cognitive deficits but not their emotional alterations.

DISCUSSION

In this study, we demonstrate that transient reprogramming with YFs not only safely increases neural proliferation during mouse brain development but also prevents the development of AD-related features in adulthood. The increased proliferation leads to more neurons and glial cells, expanding the cortex and improving behavioral performance. At adult stages, we found that principal neurons in the hippocampus tolerate transient YF expression for several months. Instead, the expression of YFs prevented the development of several AD-related hallmarks and ameliorated some of the cognitive deficits in the 5xFAD mouse model. These findings enhance our understanding of YFs as a tool to modulate neural proliferation and highlight their potential use in brain disorders.

Cortical expansion by transient YF expression

We show that long-term or strong induction of YFs during development can affect cell fate, as evidenced by the loss of identity markers in progenitors and neurons, and the emergence of Nanog expression. This extends the concept that strong and continued overexpression of YFs can induce pluripotency *in vivo*.[3,17] Interestingly, low and transient YF induction is tolerated during brain development.

In the cortex, we identified two additional cell populations following transient YF expression during development, comprising neurons and APs enriched with Oct4. Cells within these clusters showed a more immature phenotype as compared with that of their control populations. This suggests that their identity is temporarily perturbed by the coexpression of YFs, but it is not lost. This observation agrees with the notion that transient de-differentiation is proposed as an integral step in the reprogramming process.[56,57] Indeed, recent studies using transient reprogramming protocols show that although cells display a temporary identity perturbation upon YF expression, they eventually recover it. This is likely due to epigenetic memory or persistent expression of specific identity genes.[58,59] Our scRNA-seq analysis showed expanded APs after YF induction, leading to more cells in the S and G2/M phase, with a proportional reduction in G1. The increased proliferation supports the finding of more upper cortical neurons and glia at adult stages, and it aligns with recent studies where partial reprogramming reactivated aged aligodendrocyte precursors[60] and increased neuroblasts in old mice.[61] Moreover, the increased proliferation could be related to proteomic changes such as reduced expression of proteins involved in cell adhesion, such as Cdh8 and Neo1. Indeed, knockdown of Cdh8 in the germinal zone during development amplifies both proliferation and neuron numbers.[29] Similarly, genetic ablation of Neo1 increases proliferation.[30] Future studies will have to explore the generality of YF induction effects in other brain regions during development.

The finding that transient reprogramming during development leads to cortical expansion that persist into adulthood, raised the question of to what extent this could improve behavioral performance in adult mice. Most studies analyzing genes associated with cortical expansion in mouse embryos have not examined their impact on adult cognitive abilities.[62] Two recent reports, achieving around 1.2-fold increase in upper-layer neurons in adult mice, found improved hippocampus-independent memory flexibility.[63,64] We were surprised to find that our mouse model displays the strongest increase in upper cortical neurons (up to 1.4-fold) at adult stages, particularly in motor and prefrontal areas. This is consistent with the expansion of rostral cortical areas during development (Figures 2B and S2A) and with improved behavior in related tasks at adult stages. For example, we observed enhanced performance on the accelerated rotarod, a well-established paradigm for cortex-dependent motor skill learning.[65] This aligns with the increased abundance of upper-layer neurons in the motor cortex involved in motor skill acquisition.[66] Similarly, we noted improved social behavior, predominantly associated with the prefrontal cortical region,[67] which expands following transient reprogramming. Interestingly, the human prefrontal cortex is the most expanded cortical region.[68] Several studies suggest that such expansion and improved social cognition is a key step in the evolution of human intelligence.[69]

Transient YF reprogramming is protective in an AD mouse model

Previous studies have demonstrated the beneficial effects of intermittent YF expression in various contexts related to regeneration and aging.[2,5,9,70] However, none of these studies has explored its impact on mature principal neurons in the context of neurodegeneration. Our study presents a novel application

Figure 6. Amelioration of AD-related hippocampal plaque loading and proteomic signatures by YF induction

(A) Coronal hippocampal sections of i4f/5xFAD mice (−VEH and −Dox) stained for Aβ. Dorsal hippocampal CA1, CA3, DG, and motor cortex are delineated.

(B) Plaque numbers in each region from (A). n = 5–7mice/group. Three slices per mouse were used. *$p < 0.05$, **$p < 0.01$, Student's t test.

(C) Diagram of DG location for proteomic profiling.

(D) Relative protein expression levels across groups with respect to control (i4F-VEH). Protein expression based on untargeted label-free quantitation (LFQ) normalized to i4F-VEH control group (value = 1), shown in a color gradient.

(E) Network analysis of KEEG pathways of differentially expressed proteins (DEPs) of i4F/5xFAD-VEH with respect to the i4F-VEH group. Significant enriched pathways are shown. n = 4–6 mice/group.

(F) Fold enrichment analysis of pathways from (E) for VEH- and Dox-treated i4F/5xFAD mice with respect to i4F-VEH group. n = 4–6 mice/group.

(G) Cytospace network model showing protein-protein interactions (PPIs) for 103 DEPs of i4F/5xFAD-VEH with respect to i4F-VEH group rescued in i4F/5xFAD-Dox group. The color bar represents the $\log_2$ fold change protein ratios. Node color represents an increase (red) or decrease (blue) in i4F/5xFAD Dox (center) and VEH (boundary) compared with i4F-VEH (control group). Edges show PPIs from the STRING database.

(H) Scheme of DG location for DNA methylation clock. Bar charts summarizing the predicted epigenetic age in i4F and VEH-/Dox-treated i4F/5xFAD mice. n = 4–5 mice/group **$p < 0.01$, ***$p < 0.001$, two-sided Student's t test. Scale bar, 450 μm (A), 500 μm (C and H).

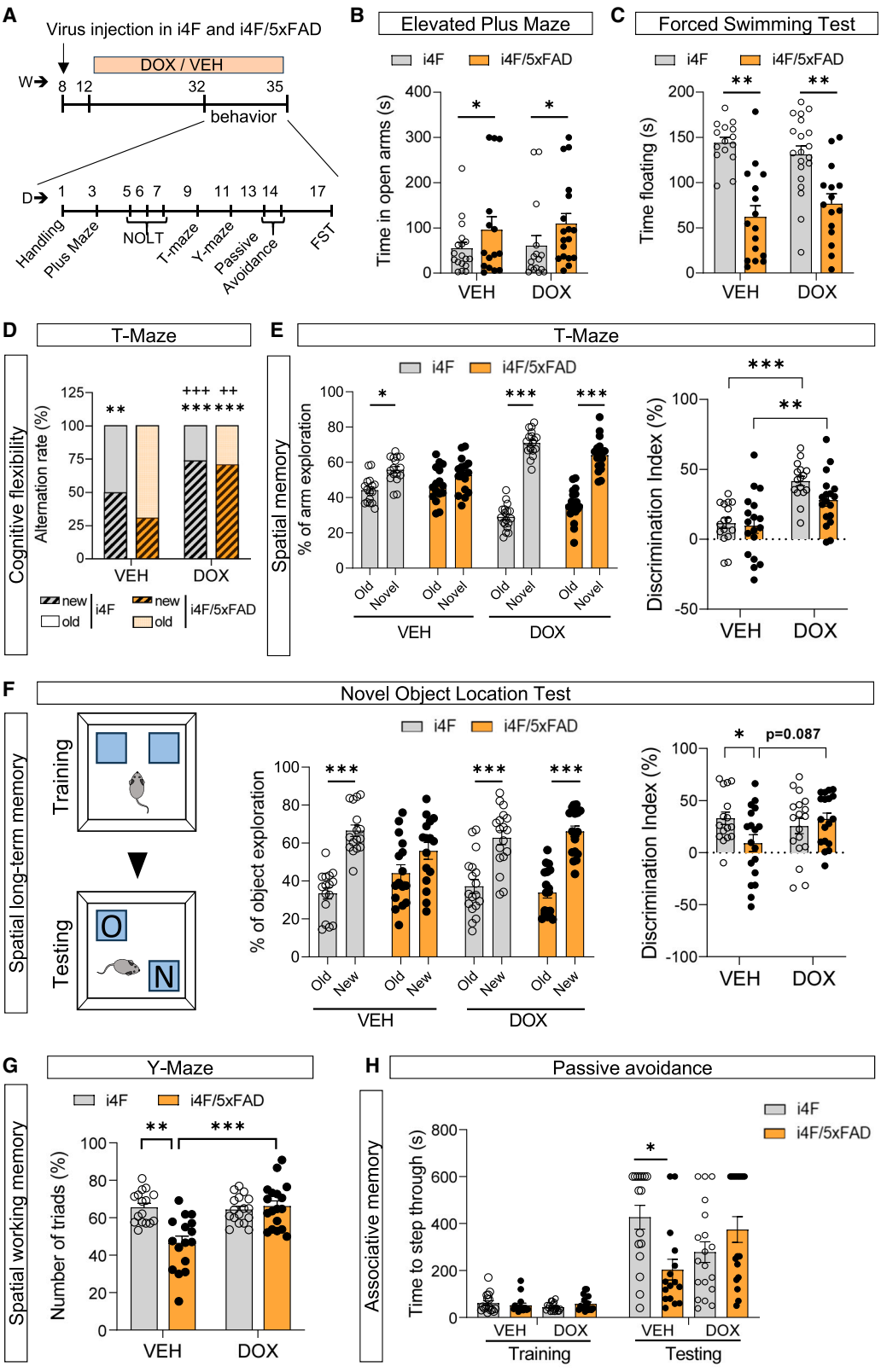

(legend on next page)

that prevents the development of several neurodegenerative hallmarks in a well-established mouse model of AD. Importantly, these improvements occurred without affecting the general health of the mice or the identity of targeted neurons in the hippocampus.

Dendritic spine pathology and the loss of synaptic contacts are defining features of neurodegenerative disorders, including AD.[71–74] Intermittent YF expression rescued synaptic features like spine and presynaptic vesicular density in granular hippocampal neurons. This result agrees with a recent observation that YF induction increases the level of the synaptic protein GluN2B in the DG.[26] This protein facilitates synaptic potentiation and promotes dendritic spine density.[75] Moreover, we observed reduced Aβ loading after YF induction in the 5xFAD mouse model. Previous studies have shown that these factors can affect the expression of several promoters, including Thy1.[59] Our results show that these effects are not due to altered expression of the APP/PSEN1 transgene or changes in the AD-related glial response. Our proteomic network analysis identified mitochondrial function and metabolism as one of the most relevant modules affected in the 5xFAD mouse model. This result is consistent with a recent transcriptomics study from human AD patients[76] and previous proteomics analyses from AD mouse models[44] and human patients.[46] One significant pathway that was rescued is related to the endocannabinoid system, which modulates Aβ loading and synaptic dysfunction.[77] Interestingly, transient YF reprogramming improved several of these proteomic AD-related signatures.

Aging influences both Aβ loading and mitochondrial function. For example, neurons are the primary source of Aβ, and its production and accumulation increase with age.[78] Aging correlates with a decline in mitochondrial function, as shown by reduced ATP production and biogenesis.[79] Given our findings that transient reprogramming improves synaptic plasticity in hippocampal neurons, combined with amelioration of Aβ loading and mitochondrial proteomic signatures in the 5xFAD mouse model, we suggest that this process may rejuvenate these neurons. This is consistent with reduced senescence markers and DNA-methylation-based epigenetic age, supporting the hypothesis that partial reprogramming can rejuvenate cells.[56,80] Our results could be an interesting starting point for further research.

This study also revealed that partial reprogramming improved some of the cognitive deficits present in the 5xFAD mouse model. This includes behavioral paradigms involving associative learning, cognitive flexibility, and spatial working memory, known to be affected in the 5xFAD mice.[81–83] These improvements are associated with YF expression in hippocampal granular and pyramidal neurons. Indeed, our proteomics analysis and histology did not identify changes in other cell populations, like microglia and astrocytes. Although YF induction in mature neurons might alter several mRNA transcription processes, as demonstrated in other systems,[84] the improvements in spine density, Aβ loading, and mitochondrial proteomic features likely contribute to better cognitive performance in the 5xFAD mouse model. It is interesting to find that in some behavioral paradigms, like cognitive flexibility, both control and 5xFAD mouse subjected to partial reprogramming outperformed their respective controls. Future studies should investigate the generality of YF induction's impact on neuronal circuits and behavior.

In conclusion, our study illustrates the potential of partial reprogramming in both promoting neurogenesis and preventing neurodegeneration. When induced during development, increased proliferation leads to expansion of the neocortex and improved behavior. At adult stages, YF expression prevents the development of several AD-related hallmarks, including some memory alterations. Our findings unveil two novel applications for partial reprogramming and pave the way for further investigations related to neuronal rejuvenation.

Limitations of the study

I4F-Rosa embryos were sensitive to Dox treatment, with only low concentrations resulting in viable embryos. Body weight increased more than brain weight, suggesting stronger YF effects in peripheral tissues, possibly related to c-Myc expression. Thus, we cannot rule out the impact of peripheral YF expression on brain development and adult behavior. To minimize this, we employed conditional Nestin-Cre-dependent expression to primarily induce YF to the central nervous system. Given that we induced all four YFs (OSKM), our findings cannot determine the individual contributions of each gene to the observed phenotypes. Regarding YF induction effects on neurodegeneration: first, our study used 5xFAD male mice, so gender-specific effects cannot be excluded. Second, because our treatment was administered to young animals before the onset of major disease hallmarks, we cannot rule out whether it resulted in the reversal or prevention of specific phenotypes. It is also possible that the effects are stronger in younger than in older mice. Also, we analyzed the animals after 5 months of treatment without examining later time points. Third, we applied the same Dox treatment in adult stages that was tolerated during development to prevent potential alterations in cell identity. However, we cannot exclude

Figure 7. YF induction prevents cognitive decline in the 5xFAD mouse model

(A) Experimental design and behavioral tests sequence.

(B) Percentage of time spent in open arms. n = 15–20 mice/group. *$p < 0.05$ between genotypes, two-way ANOVA.

(C) Time floating. n = 15–20 mice/group. **$p < 0.01$ between genotypes, two-way ANOVA.

(D) Cognitive flexibility was measured as the first arm visited in the testing trial. Alternation presented as %. n = 15–20 mice/group. **$p < 0.01$, ***$p < 0.001$ with respect to i4F/5xFAD-VEH. ++$p < 0.01$,+++ $p < 0.001$ with respect to i4F-VEH. Chi-squared test.

(E) Left panel shows the percentage of time exploring the novel vs. the old arm. n = 15–20 mice/group. *$p < 0.05$, ***$p < 0.001$. Two-way ANOVA with Bonferroni's post hoc test. Discrimination index (DI) values of the T-maze performance is shown on the right. **$p < 0.01$, ***$p < 0.001$.

(F) Percentage of time exploring the object placed in a new vs. an old location. n = 15–20 mice/group. *$p < 0.05$, ***$p < 0.001$. Two-way ANOVA with Bonferroni's post hoc test. Right graph shows the DI.

(G) Quantification of spontaneous alternation. n = 15–20mice/group. **$p < 0.01$, ***$p < 0.001$ with respect to i4F/5xFAD-VEH group.

(H) Latency (seconds) to step-through in both training and testing trial post electric shock. n = 15–20 mice/group. *p < 0.05 with respect to i4F-VEH group. Two-way ANOVA with Bonferroni's post hoc test.

the possibility of a temporary perturbation in cell identity during the 5-month treatment.

RESOURCE AVAILABILITY

Lead contact

Further information and request for resources and reagents should be directed and will be fulfilled by the lead contact, Daniel del Toro (danieldeltoro@ub.edu).

Materials availability

This study did not generate new unique reagents.

Data and code availability

- scRNA-seq data have been deposited in NCBI's Gene Expression Omnibus (GEO) and mass spectrometry data in the PRIDE repository, where they will be publicly available as of the date of publication. Accession numbers are listed in the key resources table.
- This paper does not report original code.
- Any additional information required to reanalyze the data reported in this paper is available from the lead contact upon request.

ACKNOWLEDGMENTS

We thank Maria Calvo from the Advanced Microscopy service (CCiT, UB) for help with confocal microscopy. We thank the proteomics facility of the Max Planck Institute of Biochemistry (Martinsried, Germany), Mythili Savariradjane for assistance with electron microscopy, and Steve Horvath for analyzing the epigenetic clocks. S.Z. was funded by the FPI fellowship from MCIN program. M.A. was funded by VHIO, Fero Foundation, and Milky Way Research Foundation. M.S. was funded by the IRB, "laCaixa" Foundation, and by the Milky Way Research Foundation. This work was supported by grants from MCIN/AEI /10.13039/501100011033 and PID2021-126961OB-I00 (to J.M.C.) and by European Union NextGenerationEU/PRTR: A.G.: PID2021-122258OB-I00 and CNS2022 – 135391 ("Consolidación" program). This work was also supported by the Instituto de Salud Carlos III and European Regional Development Fund (Red de Terapias Avanzadas, RD21/0017/0020 to J.M.C.); Generalitat de Catalunya (2021 SGR 01094 and 01086); "la Caixa" Foundation LCF/PR/HR21-00622 to J.M.C. and the fellowship ID 100010434 to J.A.; and the Max Planck Society (to R.K.) and the Fundación Ramón Areces (CIVP21A7024) to A.G. D.d.T. was funded by the RyC program (RYC-2017-23486), MCIN: RTI2018-095580-A-100 and PID2021-124852OB-100, and Wellcome Trust:# ALR02940.

AUTHOR CONTRIBUTIONS

Y.-R.S. led the i4F-Nes model and performed scRNA-seq and proteomics experiments. S.Z. led the behavior work of i4F-Rosa and i4F:5xFAD models. S.Z., X.B., G.S.-B., H.Y.L., I.R.-N., A.S.-B., and I.B. contributed to IF experiments. A.S.-B. performed surgeries and WB, and I.R.-N. performed RT-qPCR experiments. C.C.-D. performed electron microscopy studies. S.H.C. helped with scRNA-seq. T.S. processed scRNA-seq data and J.A. processed the cell cycle. I.M.-V., L.R., and V.G. contributed with DNA methylation clocks experiments. N.A. generated i4F-rosa embryos. J.A. and J.M.C. oversaw work related to IF and cell cycle. M.A. and M.S. provided the i4F mouse model and reprogramming expertise. R.K. oversaw the developmental studies. A.G. oversaw i4F-Rosa behavior and work related to the 5xFAD model. D.d.T. oversaw i4F-Rosa and i4F-Nes work and cell biology aspects. All authors have contributed to the manuscript.

DECLARATION OF INTERESTS

M.S. is a shareholder of Senolytic Therapeutics, Life Biosciences, Rejuveron Senescence Therapeutics, and Altos Labs. M.S. was a consultant of Rejuveron Senescence Therapeutics and Altos Labs until the end of 2022. M.A. is a shareholder of Altos Labs.

STAR★METHODS

Detailed methods are provided in the online version of this paper and include the following:

- KEY RESOURCES TABLE
- EXPERIMENTAL MODELS AND STUDY PARTICIPANT DETAILS
  - Animals
- METHOD DETAILS
  - Experimental design using AAVs
  - Stereotaxic surgeries and viral constructs
  - Behavioural assessments
  - Golgi Staining and dendritic spine density analysis
  - Immunohistochemistry
  - Electron microscope experiments
  - Mass spectrometry experiments
  - Cleared whole-mount embryonic brain
  - Single-cell dissociation and Single-cell RNA-seq
  - Single-cell RNA-seq data processing
  - DNA methylation Clock
  - In utero electroporation
  - Western blot
  - EdU and BrdU
  - RNA isolation and RT-qPCR
- QUANTIFICATION AND STATISTICAL ANALYSIS

SUPPLEMENTAL INFORMATION

Supplemental information can be found online at https://doi.org/10.1016/j.stem.2024.09.013.

Received: November 2, 2023
Revised: July 8, 2024
Accepted: September 18, 2024
Published: October 18, 2024

REFERENCES

1. Takahashi, K., and Yamanaka, S. (2006). Induction of pluripotent stem cells from mouse embryonic and adult fibroblast cultures by defined factors. Cell *126*, 663–676. https://doi.org/10.1016/J.CELL.2006.07.024.
2. Ocampo, A., Reddy, P., Martinez-Redondo, P., Platero-Luengo, A., Hatanaka, F., Hishida, T., Li, M., Lam, D., Kurita, M., Beyret, E., et al. (2016). In Vivo Amelioration of Age-Associated Hallmarks by Partial Reprogramming. Cell *167*, 1719–1733.e12. https://doi.org/10.1016/j.cell.2016.11.052.
3. Chondronasiou, D., Gill, D., Mosteiro, L., Urdinguio, R.G., Berenguer-Llergo, A., Aguilera, M., Durand, S., Aprahamian, F., Nirmalathasan, N., Abad, M., et al. (2022). Multi-omic rejuvenation of naturally aged tissues by a single cycle of transient reprogramming. Aging Cell *21*, e13578. https://doi.org/10.1111/ACEL.13578.
4. Sarkar, T.J., Quarta, M., Mukherjee, S., Colville, A., Paine, P., Doan, L., Tran, C.M., Chu, C.R., Horvath, S., Qi, L.S., et al. (2020). Transient non-integrative expression of nuclear reprogramming factors promotes multifaceted amelioration of aging in human cells. Nat. Commun. *11*, 1545. https://doi.org/10.1038/S41467-020-15174-3.
5. Lu, Y., Brommer, B., Tian, X., Krishnan, A., Meer, M., Wang, C., Vera, D.L., Zeng, Q., Yu, D., Bonkowski, M.S., et al. (2020). Reprogramming to recover youthful epigenetic information and restore vision. Nature *588*, 124–129. https://doi.org/10.1038/S41586-020-2975-4.
6. Yang, J.H., Hayano, M., Griffin, P.T., Amorim, J.A., Bonkowski, M.S., Apostolides, J.K., Salfati, E.L., Blanchette, M., Munding, E.M., Bhakta, M., et al. (2023). Loss of epigenetic information as a cause of mammalian aging. Cell *186*, 305–326.e27. https://doi.org/10.1016/J.CELL.2022.12.027.
7. Zhang, W., Li, J., Suzuki, K., Qu, J., Wang, P., Zhou, J., Liu, X., Ren, R., Xu, X., Ocampo, A., et al. (2015). Aging stem cells. A Werner syndrome stem

cell model unveils heterochromatin alterations as a driver of human aging. Science *348*, 1160–1163. https://doi.org/10.1126/SCIENCE.AAA1356.

8. Mahmoudi, S., and Brunet, A. (2012). Aging and reprogramming: a two-way street. Curr. Opin. Cell Biol. *24*, 744–756. https://doi.org/10.1016/J.CEB.2012.10.004.

9. Browder, K.C., Reddy, P., Yamamoto, M., Haghani, A., Guillen, I.G., Sahu, S., Wang, C., Luque, Y., Prieto, J., Shi, L., et al. (2022). In vivo partial reprogramming alters age-associated molecular changes during physiological aging in mice. Nat. Aging *2*, 243–253. https://doi.org/10.1038/s43587-022-00183-2.

10. Hishida, T., Yamamoto, M., Hishida-Nozaki, Y., Shao, C., Huang, L., Wang, C., Shojima, K., Xue, Y., Hang, Y., Shokhirev, M., et al. (2022). In vivo partial cellular reprogramming enhances liver plasticity and regeneration. Cell Rep. *39*, 110730. https://doi.org/10.1016/J.CELREP.2022.110730.

11. Wang, C., Rabadan Ros, R., Martinez-Redondo, P., Ma, Z., Shi, L., Xue, Y., Guillen-Guillen, I., Huang, L., Hishida, T., Liao, H.K., et al. (2021). In vivo partial reprogramming of myofibers promotes muscle regeneration by remodeling the stem cell niche. Nat. Commun. *12*, 3094. https://doi.org/10.1038/S41467-021-23353-Z.

12. Farber, G., Liu, J., and Qian, L. (2022). OSKM-mediated reversible reprogramming of cardiomyocytes regenerates injured myocardium. Cell Regen. *11*, 6. https://doi.org/10.1186/S13619-021-00106-3.

13. Chen, Y., Lüttmann, F.F., Schoger, E., Schöler, H.R., Zelarayán, L.C., Kim, K.P., Haigh, J.J., Kim, J., and Braun, T. (2021). Reversible reprogramming of cardiomyocytes to a fetal state drives heart regeneration in mice. Science *373*, 1537–1540. https://doi.org/10.1126/SCIENCE.ABG5159.

14. Chondronasiou, D., Martínez de Villarreal, J., Melendez, E., Lynch, C.J., del Pozo, N.D., Kovatcheva, M., Aguilera, M., Prats, N., Real, F.X., and Serrano, M. (2022). Deciphering the roadmap of in vivo reprogramming toward pluripotency. Stem Cell Rep. *17*, 2501–2517. https://doi.org/10.1016/J.STEMCR.2022.09.009.

15. Tran, K.A., Pietrzak, S.J., Zaidan, N.Z., Siahpirani, A.F., McCalla, S.G., Zhou, A.S., Iyer, G., Roy, S., and Sridharan, R. (2019). Defining Reprogramming Checkpoints from Single-Cell Analyses of Induced Pluripotency. Cell Rep. *27*, 1726–1741.e5. https://doi.org/10.1016/J.CELREP.2019.04.056.

16. Maza, I., Caspi, I., Zviran, A., Chomsky, E., Rais, Y., Viukov, S., Geula, S., Buenrostro, J.D., Weinberger, L., Krupalnik, V., et al. (2015). Transient acquisition of pluripotency during somatic cell transdifferentiation with iPSC reprogramming factors. Nat. Biotechnol. *33*, 769–774. https://doi.org/10.1038/NBT.3270.

17. Abad, M., Mosteiro, L., Pantoja, C., Cañamero, M., Rayon, T., Ors, I., Graña, O., Megías, D., Domínguez, O., Martínez, D., et al. (2013). Reprogramming in vivo produces teratomas and iPS cells with totipotency features. Nature *502*, 340–345. https://doi.org/10.1038/nature12586.

18. Xia, X., Jiang, Q., McDermott, J., and Han, J.J. (2018). Aging and Alzheimer's disease: Comparison and associations from molecular to system level. Aging Cell *17*, e12802. https://doi.org/10.1111/ACEL.12802.

19. Cai, H., Cong, W.N., Ji, S., Rothman, S., Maudsley, S., and Martin, B. (2012). Metabolic Dysfunction in Alzheimer's Disease and Related Neurodegenerative Disorders. Curr. Alzheimer Res. *9*, 5–17. https://doi.org/10.2174/156720512799015064.

20. Huang, W.-J., Zhang, X., and Chen, W.-W. (2016). Role of oxidative stress in Alzheimer's disease. Biomed. Rep. *4*, 519–522. https://doi.org/10.3892/br.2016.630.

21. Reza-Zaldivar, E.E., Hernández-Sápiens, M.A., Minjarez, B., Gómez-Pinedo, U., Sánchez-González, V.J., Márquez-Aguirre, A.L., and Canales-Aguirre, A.A. (2020). Dendritic Spine and Synaptic Plasticity in Alzheimer's Disease: A Focus on MicroRNA. Front. Cell Dev. Biol. *8*, 255. https://doi.org/10.3389/fcell.2020.00255.

22. Yang, S.G., Wang, X.W., Qian, C., and Zhou, F.Q. (2022). Reprogramming neurons for regeneration: the fountain of youth. Prog. Neurobiol. *214*, 102284. https://doi.org/10.1016/J.PNEUROBIO.2022.102284.

23. Valadez-Barba, V., Cota-Coronado, A., Hernández-Pérez, O.R., Lugo-Fabres, P.H., Padilla-Camberos, E., Díaz, N.F., and Díaz-Martínez, N.E. (2020). iPSC for modeling neurodegenerative disorders. Regen. Ther. *15*, 332–339. https://doi.org/10.1016/J.RETH.2020.11.006.

24. Brot, S., Thamrin, N.P., Bonnet, M.L., Francheteau, M., Patrigeon, M., Belnoue, L., and Gaillard, A. (2022). Long-Term Evaluation of Intranigral Transplantation of Human iPSC-Derived Dopamine Neurons in a Parkinson's Disease Mouse Model. Cells *11*, 1596. https://doi.org/10.3390/CELLS11101596.

25. Han, F., Wang, W., Chen, B., Chen, C., Li, S., Lu, X., Duan, J., Zhang, Y., Zhang, Y.A., Guo, W., et al. (2015). Human induced pluripotent stem cell-derived neurons improve motor asymmetry in a 6-hydroxydopamine-induced rat model of Parkinson's disease. Cytotherapy *17*, 665–679. https://doi.org/10.1016/J.JCYT.2015.02.001.

26. Rodríguez-Matellán, A., Alcazar, N., Hernández, F., Serrano, M., and Ávila, J. (2020). In Vivo Reprogramming Ameliorates Aging Features in Dentate Gyrus Cells and Improves Memory in Mice. Stem Cell Rep. *15*, 1056–1066. https://doi.org/10.1016/j.stemcr.2020.09.010.

27. Zalc, A., Sinha, R., Gulati, G.S., Wesche, D.J., Daszczuk, P., Swigut, T., Weissman, I.L., and Wysocka, J. (2021). Reactivation of the pluripotency program precedes formation of the cranial neural crest. Science *371*, eabb4776. https://doi.org/10.1126/science.abb4776.

28. Ohnishi, K., Semi, K., Yamamoto, T., Shimizu, M., Tanaka, A., Mitsunaga, K., Okita, K., Osafune, K., Arioka, Y., Maeda, T., et al. (2014). Premature termination of reprogramming in vivo leads to cancer development through altered epigenetic regulation. Cell *156*, 663–677. https://doi.org/10.1016/j.cell.2014.01.005.

29. Memi, F., Killen, A.C., Barber, M., Parnavelas, J.G., and Andrews, W.D. (2019). Cadherin 8 regulates proliferation of cortical interneuron progenitors. Brain Struct. Funct. *224*, 277–292. https://doi.org/10.1007/s00429-018-1772-4.

30. Kam, J.W.K., Dumontier, E., Baim, C., Brignall, A.C., Mendes da Silva, D.M., Cowan, M., Kennedy, T.E., and Cloutier, J.F. (2016). RGMB and neogenin control cell differentiation in the developing olfactory epithelium. Development *143*, 1534–1546. https://doi.org/10.1242/DEV.118638.

31. Di Bella, D.J., Habibi, E., Stickels, R.R., Scalia, G., Brown, J., Yadollahpour, P., Yang, S.M., Abbate, C., Biancalani, T., Macosko, E.Z., et al. (2021). Molecular Logic of Cellular Diversification in the Mouse Cerebral Cortex. Nature *595*, 554–559. https://doi.org/10.1038/S41586-021-03670-5.

32. Ge, S.X., Jung, D., and Yao, R. (2020). ShinyGO: a graphical gene-set enrichment tool for animals and plants. Bioinformatics *36*, 2628–2629. https://doi.org/10.1093/BIOINFORMATICS/BTZ931.

33. Riba, A., Oravecz, A., Durik, M., Jiménez, S., Alunni, V., Cerciat, M., Jung, M., Keime, C., Keyes, W.M., and Molina, N. (2022). Cell cycle gene regulation dynamics revealed by RNA velocity and deep-learning. Nat. Commun. *13*, 2865. https://doi.org/10.1038/s41467-022-30545-8.

34. Borrell, V., and Götz, M. (2014). Role of radial glial cells in cerebral cortex folding. Curr. Opin. Neurobiol. *27*, 39–46. https://doi.org/10.1016/j.conb.2014.02.007.

35. Galakhova, A.A., Hunt, S., Wilbers, R., Heyer, D.B., de Kock, C.P.J., Mansvelder, H.D., and Goriounova, N.A. (2022). Evolution of cortical neurons supporting human cognition. Trends Cogn. Sci. *26*, 909–922. https://doi.org/10.1016/J.TICS.2022.08.012.

36. Fernández, V., Llinares-Benadero, C., and Borrell, V. (2016). Cerebral cortex expansion and folding: what have we learned? EMBO J. *35*, 1021–1044. https://doi.org/10.15252/embj.201593701.

37. Lee, C., Kim, Y., and Kaang, B.K. (2022). The Primary Motor Cortex: The Hub of Motor Learning in Rodents. Neuroscience *485*, 163–170. https://doi.org/10.1016/J.NEUROSCIENCE.2022.01.009.

38. Levy, D.R., Tamir, T., Kaufman, M., Parabucki, A., Weissbrod, A., Schneidman, E., and Yizhar, O. (2019). Dynamics of social representation in the mouse prefrontal cortex. Nat. Neurosci. *22*, 2013–2022. https://doi.org/10.1038/s41593-019-0531-z.

39. Shiotsuki, H., Yoshimi, K., Shimo, Y., Funayama, M., Takamatsu, Y., Ikeda, K., Takahashi, R., Kitazawa, S., and Hattori, N. (2010). A rotarod test for evaluation of motor skill learning. J. Neurosci. Methods *189*, 180–185. https://doi.org/10.1016/J.JNEUMETH.2010.03.026.

40. Kedia, S., and Chattarji, S. (2014). Marble burying as a test of the delayed anxiogenic effects of acute immobilisation stress in mice. J. Neurosci. Methods *233*, 150–154. https://doi.org/10.1016/J.JNEUMETH.2014.06.012.

41. Yang, M., Silverman, J.L., and Crawley, J.N. (2011). Automated Three-Chambered Social Approach Task for Mice. Curr. Protoc. Neurosci. *Chapter 8*, Unit.8.26. https://doi.org/10.1002/0471142301.NS0826S56.

42. Oakley, H., Cole, S.L., Logan, S., Maus, E., Shao, P., Craft, J., Guillozet-Bongaarts, A., Ohno, M., Disterhoft, J., Van Eldik, L., et al. (2006). Intraneuronal beta-amyloid aggregates, neurodegeneration, and neuron loss in transgenic mice with five familial Alzheimer's disease mutations: potential factors in amyloid plaque formation. J. Neurosci. *26*, 10129–10140. https://doi.org/10.1523/JNEUROSCI.1202-06.2006.

43. De Pins, B., Cifuentes-Díaz, C., Farah, A.T., López-Molina, L., Montalban, E., Sancho-Balsells, A., López, A., Ginés, S., Delgado-García, J.M., Alberch, J., et al. (2019). Conditional BDNF Delivery from Astrocytes Rescues Memory Deficits, Spine Density, and Synaptic Properties in the 5xFAD Mouse Model of Alzheimer Disease. J. Neurosci. *39*, 2441–2458. https://doi.org/10.1523/JNEUROSCI.2121-18.2019.

44. Kim, D.K., Han, D., Park, J., Choi, H., Park, J.C., Cha, M.Y., Woo, J., Byun, M.S., Lee, D.Y., Kim, Y., et al. (2019). Deep proteome profiling of the hippocampus in the 5XFAD mouse model reveals biological process alterations and a novel biomarker of Alzheimer's disease. Exp. Mol. Med. *51*, 1–17. https://doi.org/10.1038/S12276-019-0326-Z.

45. Babcock, K.R., Page, J.S., Fallon, J.R., and Webb, A.E. (2021). Adult Hippocampal Neurogenesis in Aging and Alzheimer's Disease. Stem Cell Rep. *16*, 681–693. https://doi.org/10.1016/J.STEMCR.2021.01.019.

46. Johnson, E.C.B., Dammer, E.B., Duong, D.M., Ping, L., Zhou, M., Yin, L., Higginbotham, L.A., Guajardo, A., White, B., Troncoso, J.C., et al. (2020). Large-scale proteomic analysis of Alzheimer's disease brain and cerebrospinal fluid reveals early changes in energy metabolism associated with microglia and astrocyte activation. Nat. Med. *26*, 769–780. https://doi.org/10.1038/S41591-020-0815-6.

47. Shannon, P., Markiel, A., Ozier, O., Baliga, N.S., Wang, J.T., Ramage, D., Amin, N., Schwikowski, B., and Ideker, T. (2003). Cytoscape: a software environment for integrated models of biomolecular interaction networks. Genome Res. *13*, 2498–2504. https://doi.org/10.1101/GR.1239303.

48. Arneson, A., Haghani, A., Thompson, M.J., Pellegrini, M., Kwon, S.B., Vu, H., Maciejewski, E., Yao, M., Li, C.Z., Lu, A.T., et al. (2022). A mammalian methylation array for profiling methylation levels at conserved sequences. Nat. Commun. *13*, 783. https://doi.org/10.1038/s41467-022-28355-z.

49. Mozhui, K., Lu, A.T., Li, C.Z., Haghani, A., Sandoval-Sierra, J.V., Wu, Y., Williams, R.W., and Horvath, S. (2022). Genetic loci and metabolic states associated with murine epigenetic aging. eLife *11*, e75244. https://doi.org/10.7554/eLife.75244.

50. Lee, M.Y., Lee, J., Hyeon, S.J., Cho, H., Hwang, Y.J., Shin, J.Y., McKee, A.C., Kowall, N.W., Il Kim, J.I., Stein, T.D., et al. (2020). Epigenome signatures landscaped by histone H3K9me3 are associated with the synaptic dysfunction in Alzheimer's disease. Aging Cell *19*, e13153. https://doi.org/10.1111/ACEL.13153.

51. Griñán-Ferré, C., Sarroca, S., Ivanova, A., Puigoriol-Illamola, D., Aguado, F., Camins, A., Sanfeliu, C., and Pallàs, M. (2016). Epigenetic mechanisms underlying cognitive impairment and Alzheimer disease hallmarks in 5XFAD mice. Aging *8*, 664–684. https://doi.org/10.18632/AGING.100906.

52. Schneider, F., Baldauf, K., Wetzel, W., and Reymann, K.G. (2015). Effects of methylphenidate on the behavior of male 5xFAD mice. Pharmacol. Biochem. Behav. *128*, 68–77. https://doi.org/10.1016/J.PBB.2014.11.006.

53. Devi, L., and Ohno, M. (2015). TrkB reduction exacerbates Alzheimer's disease-like signaling aberrations and memory deficits without affecting β-amyloidosis in 5XFAD mice. Transl. Psychiatry *5*, e562. https://doi.org/10.1038/TP.2015.55.

54. Fanselow, M.S., and Dong, H.W. (2010). Are The Dorsal and Ventral Hippocampus functionally distinct structures? Neuron *65*, 7–19. https://doi.org/10.1016/J.NEURON.2009.11.031.

55. Lalonde, R. (2002). The neurobiological basis of spontaneous alternation. Neurosci. Biobehav. Rev. *26*, 91–104. https://doi.org/10.1016/S0149-7634(01)00041-0.

56. Singh, P.B., and Zhakupova, A. (2022). Age reprogramming: cell rejuvenation by partial reprogramming. Development *149*, dev200755. https://doi.org/10.1242/dev.200755.

57. Manukyan, M., and Singh, P.B. (2012). Epigenetic rejuvenation. Genes Cells *17*, 337–343. https://doi.org/10.1111/J.1365-2443.2012.01595.X.

58. Gill, D., Parry, A., Santos, F., Okkenhaug, H., Todd, C.D., Hernando-Herraez, I., Stubbs, T.M., Milagre, I., and Reik, W. (2022). Multi-omic rejuvenation of human cells by maturation phase transient reprogramming. eLife *11*, e71624. https://doi.org/10.7554/eLife.71624.

59. Roux, A.E., Zhang, C., Paw, J., Zavala-Solorio, J., Malahias, E., Vijay, T., Kolumam, G., Kenyon, C., and Kimmel, J.C. (2022). Diverse partial reprogramming strategies restore youthful gene expression and transiently suppress cell identity. Cell Syst. *13*, 574–587.e11. https://doi.org/10.1016/j.cels.2022.05.002.

60. Neumann, B., Segel, M., Ghosh, T., Zhao, C., Tourlomousis, P., Young, A., Förster, S., Sharma, A., Chen, C.Z.Y., Cubillos, J.F., et al. (2021). Myc determines the functional age state of oligodendrocyte progenitor cells. Nat Aging *1*, 826–837. https://doi.org/10.1038/S43587-021-00109-4.

61. Xu, L., Ramirez-Matias, J., Hauptschein, M., Sun, E.D., Lunger, J.C., Buckley, M.T., and Brunet, A. (2024). Restoration of neuronal progenitors by partial reprogramming in the aged neurogenic niche. Nat Aging *4*, 546–567. https://doi.org/10.1038/S43587-024-00594-3.

62. Llinares-Benadero, C., and Borrell, V. (2019). Deconstructing cortical folding: genetic, cellular and mechanical determinants. Nat. Rev. Neurosci. *20*, 161–176. https://doi.org/10.1038/s41583-018-0112-2.

63. Zhao, J., Feng, C., Wang, W., Su, L., and Jiao, J. (2022). Human SERPINA3 induces neocortical folding and improves cognitive ability in mice. Cell Discov. *8*, 124. https://doi.org/10.1038/S41421-022-00469-0.

64. Xing, L., Kubik-Zahorodna, A., Namba, T., Pinson, A., Florio, M., Prochazka, J., Sarov, M., Sedlacek, R., and Huttner, W.B. (2021). Expression of human-specific ARHGAP11B in mice leads to neocortex expansion and increased memory flexibility. EMBO J. *40*, e107093. https://doi.org/10.15252/EMBJ.2020107093.

65. Buitrago, M.M., Schulz, J.B., Dichgans, J., and Luft, A.R. (2004). Short and long-term motor skill learning in an accelerated rotarod training paradigm. Neurobiol. Learn. Mem. *81*, 211–216. https://doi.org/10.1016/J.NLM.2004.01.001.

66. Kawai, R., Markman, T., Poddar, R., Ko, R., Fantana, A.L., Dhawale, A.K., Kampff, A.R., and Ölveczky, B.P. (2015). Motor cortex is required for learning but not for executing a motor skill. Neuron *86*, 800–812. https://doi.org/10.1016/J.NEURON.2015.03.024.

67. Bicks, L.K., Koike, H., Akbarian, S., and Morishita, H. (2015). Prefrontal cortex and social cognition in mouse and man. Front. Psychol. *6*, 166005. https://doi.org/10.3389/fpsyg.2015.01805.

68. Smaers, J.B., Gómez-Robles, A., Parks, A.N., and Sherwood, C.C. (2017). Exceptional Evolutionary Expansion of Prefrontal Cortex in Great Apes and Humans. Curr. Biol. *27*, 714–720. https://doi.org/10.1016/J.CUB.2017.01.020.

69. Kamil, A.C. (2004). Sociality and the evolution of intelligence. Trends Cogn. Sci. *8*, 195–197. https://doi.org/10.1016/j.tics.2004.03.002.

70. Doeser, M.C., Schöler, H.R., and Wu, G. (2018). Reduction of Fibrosis and Scar Formation by Partial Reprogramming In Vivo. Stem Cells *36*, 1216–1225. https://doi.org/10.1002/STEM.2842.

71. Dorostkar, M.M., Zou, C., Blazquez-Llorca, L., and Herms, J. (2015). Analyzing dendritic spine pathology in Alzheimer's disease: problems

and opportunities. Acta Neuropathol. *130*, 1–19. https://doi.org/10.1007/S00401-015-1449-5.

72. Yuki, D., Sugiura, Y., Zaima, N., Akatsu, H., Takei, S., Yao, I., Maesako, M., Kinoshita, A., Yamamoto, T., Kon, R., et al. (2014). DHA-PC and PSD-95 decrease after loss of synaptophysin and before neuronal loss in patients with Alzheimer's disease. Sci. Rep. *4*, 7130. https://doi.org/10.1038/SREP07130.
73. Crowe, S.E., and Ellis-Davies, G.C.R. (2014). Spine pruning in 5xFAD mice starts on basal dendrites of layer 5 pyramidal neurons. Brain Struct. Funct. *219*, 571–580. https://doi.org/10.1007/S00429-013-0518-6.
74. Hongpaisan, J., Sun, M.K., and Alkon, D.L. (2011). PKC ε activation prevents synaptic loss, Aβ elevation, and cognitive deficits in Alzheimer's disease transgenic mice. J. Neurosci. *31*, 630–643. https://doi.org/10.1523/JNEUROSCI.5209-10.2011.
75. Brigman, J.L., Wright, T., Talani, G., Prasad-Mulcare, S., Jinde, S., Seabold, G.K., Mathur, P., Davis, M.I., Bock, R., Gustin, R.M., et al. (2010). Loss of GluN2B-containing NMDA receptors in CA1 hippocampus and cortex impairs long-term depression, reduces dendritic spine density, and disrupts learning. J. Neurosci. *30*, 4590–4600. https://doi.org/10.1523/JNEUROSCI.0640-10.2010.
76. Mathys, H., Peng, Z., Boix, C.A., Victor, M.B., Leary, N., Babu, S., Abdelhady, G., Jiang, X., Ng, A.P., Ghafari, K., et al. (2023). Single-cell atlas reveals correlates of high cognitive function, dementia, and resilience to Alzheimer's disease pathology. Cell *186*, 4365–4385.e27. https://doi.org/10.1016/J.CELL.2023.08.039.
77. Mulder, J., Zilberter, M., Pasquaré, S.J., Alpár, A., Schulte, G., Ferreira, S.G., Köfalvi, A., Martín-Moreno, A.M., Keimpema, E., Tanila, H., et al. (2011). Molecular reorganization of endocannabinoid signalling in Alzheimer's disease. Brain *134*, 1041–1060. https://doi.org/10.1093/BRAIN/AWR046.
78. Burrinha, T., Martinsson, I., Gomes, R., Terrasso, A.P., Gouras, G.K., and Almeida, C.G. (2021). Upregulation of APP endocytosis by neuronal aging drives amyloid-dependent synapse loss. J. Cell Sci. *134*, jcs255752. https://doi.org/10.1242/JCS.255752.
79. Sun, N., Youle, R.J., and Finkel, T. (2016). The Mitochondrial Basis of Aging. Mol. Cell *61*, 654–666. https://doi.org/10.1016/J.MOLCEL.2016.01.028.
80. López-Otín, C., Blasco, M.A., Partridge, L., Serrano, M., and Kroemer, G. (2023). Hallmarks of aging: An expanding universe. Cell *186*, 243–278. https://doi.org/10.1016/J.CELL.2022.11.001.
81. Montalban, E., Al-Massadi, O., Sancho-Balsells, A., Brito, V., de Pins, B., Alberch, J., Ginés, S., Girault, J.A., and Giralt, A. (2019). Pyk2 in the amygdala modulates chronic stress sequelae via PSD-95-related micro-structural changes. Transl. Psychiatry *9*, 3. https://doi.org/10.1038/s41398-018-0352-y.
82. Giralt, A., de Pins, B., Cifuentes-Díaz, C., López-Molina, L., Farah, A.T., Tible, M., Deramecourt, V., Arold, S.T., Ginés, S., Hugon, J., et al. (2018). PTK2B/Pyk2 overexpression improves a mouse model of Alzheimer's disease. Exp. Neurol. *307*, 62–73. https://doi.org/10.1016/J.EXPNEUROL.2018.05.020.
83. Pérez-Sisqués, L., Sancho-Balsells, A., Solana-Balaguer, J., Campoy-Campos, G., Vives-Isern, M., Soler-Palazón, F., Anglada-Huguet, M., López-Toledano, M.-Á., Mandelkow, E.-M., Alberch, J., et al. (2021). RTP801/REDD1 contributes to neuroinflammation severity and memory impairments in Alzheimer's disease. Cell Death Dis. *12*, 616. https://doi.org/10.1038/s41419-021-03899-y.
84. Sridharan, R., Tchieu, J., Mason, M.J., Yachechko, R., Kuoy, E., Horvath, S., Zhou, Q., and Plath, K. (2009). Role of the murine reprogramming factors in the induction of pluripotency. Cell *136*, 364–377. https://doi.org/10.1016/J.CELL.2009.01.001.
85. Tronche, F., Kellendonk, C., Kretz, O., Gass, P., Anlag, K., Orban, P.C., Bock, R., Klein, R., and Schütz, G. (1999). Disruption of the glucocorticoid receptor gene in the nervous system results in reduced anxiety. Nat. Genet. *23*, 99–103. https://doi.org/10.1038/12703.
86. Cacchiarelli, D., Trapnell, C., Ziller, M.J., Soumillon, M., Cesana, M., Karnik, R., Donaghey, J., Smith, Z.D., Ratanasirintrawoot, S., Zhang, X., et al. (2015). Integrative Analyses of Human Reprogramming Reveal Dynamic Nature of Induced Pluripotency. Cell *162*, 412–424. https://doi.org/10.1016/J.CELL.2015.06.016.
87. Aihara, S., Fujimoto, S., Sakaguchi, R., and Imai, T. (2021). BMPR-2 gates activity-dependent stabilization of primary dendrites during mitral cell remodeling. Cell Rep *35*. https://doi.org/10.1016/J.CELREP.2021.109276.
88. Schindelin, J., Arganda-Carreras, I., Frise, E., Kaynig, V., Longair, M., Pietzsch, T., Preibisch, S., Rueden, C., Saalfeld, S., Schmid, B., et al. (2012). Fiji: an open-source platform for biological-image analysis. Nature Methods *9*, 676–682. https://doi.org/10.1038/nmeth.2019.
89. Giralt, A., Brito, V., Chevy, Q., Simonnet, C., Otsu, Y., Cifuentes-Díaz, C., de Pins, B., Coura, R., Alberch, J., Ginés, S., et al. (2017). Pyk2 modulates hippocampal excitatory synapses and contributes to cognitive deficits in a Huntington's disease model. Nat. Commun. *8*, 15592. https://doi.org/10.1038/ncomms15592.
90. Schneider, C.A., Rasband, W.S., and Eliceiri, K.W. (2012). NIH Image to ImageJ: 25 years of image analysis. Nat. Methods *9*, 671–675. https://doi.org/10.1038/nmeth.2089.
91. Carpenter, A.E., Jones, T.R., Lamprecht, M.R., Clarke, C., Kang, I.H., Friman, O., Guertin, D.A., Chang, J.H., Lindquist, R.A., Moffat, J., et al. (2006). CellProfiler: Image analysis software for identifying and quantifying cell phenotypes. Genome Biol. *7*, R100. https://doi.org/10.1186/gb-2006-7-10-r100.
92. Sancho-Balsells, A., Borràs-Pernas, S., Flotta, F., Chen, W., del Toro, D., Rodríguez, M.J., Alberch, J., Blivet, G., Touchon, J., Xifró, X., et al. (2024). Brain–gut photobiomodulation restores cognitive alterations in chronically stressed mice through the regulation of Sirt1 and neuroinflammation. J. Affect. Disord. *354*, 574–588. https://doi.org/10.1016/J.JAD.2024.03.075.
93. Susaki, E.A., Tainaka, K., Perrin, D., Kishino, F., Tawara, T., Watanabe, T.M., Yokoyama, C., Onoe, H., Eguchi, M., Yamaguchi, S., et al. (2014). Whole-brain imaging with single-cell resolution using chemical cocktails and computational analysis. Cell *157*, 726–739. https://doi.org/10.1016/j.cell.2014.03.042.
94. Yang, B., Treweek, J.B., Kulkarni, R.P., Deverman, B.E., Chen, C.K., Lubeck, E., Shah, S., Cai, L., and Gradinaru, V. (2014). Single-cell phenotyping within transparent intact tissue through whole-body clearing. Cell *158*, 945–958. https://doi.org/10.1016/J.CELL.2014.07.017.
95. Zhou, W., Triche, T.J., Laird, P.W., and Shen, H. (2018). SeSAMe: reducing artifactual detection of DNA methylation by Infinium BeadChips in genomic deletions. Nucleic Acids Res *46*. https://doi.org/10.1093/NAR/GKY691.

STAR★METHODS

KEY RESOURCES TABLE

REAGENT or RESOURCE	SOURCE	IDENTIFIER
Antibodies		
Rabbit anti SATB2	Abcam	Cat # AB34735; RRID:AB_2301417
Rat anti Ctip2	Abcam	Cat # AB18465; RRID:AB_2064130
Rabbit anti-Oct3/4	BD Biosciences	Cat # 611202; RRID:AB_398736
Rabbit anti-Nanog	Novus Biologicals	Cat # NB100-58842; RRID:AB_877697
Mouse anti-Myc	Santa Cruz	Cat # SC-40; RRID:AB_627268
Rabbit anti-Pax6	BioLegend	Cat # 901301; RRID:AB_2565003
Goat anti Sox2	R&D Systems	Cat # AF2018; RRID:AB_355110H3
Rat anti Histone H3	Abcam	Cat # AB10543; RRID:AB_2295065
Rat anti BrdU	Abcam	Cat # AB6326; RRID:AB_305426
Mouse anti-Pvim	Abcam	Cat # AB20346; RRID:AB_445527
Rabbit anti-Sirt1	Cell Signaling	CAT #2028; RRID:AB_1196631
Rabbit anti-GFAP	DAKO	CAT #z0334; RRID:AB_10013382
Goat anti-Iba1	Abcam	CAT #Ab5076 RRID:AB_2224402
Rabbit anti-APP	Novus Biologicals	CAT #NBP2-62566; RRID:AB_2917960
Mouse anti-NeuN	Chemicon	CAT #MAB377; RRID:AB_2298772
Rabbit anti-Pyk2	Sigma	CAT #P3902 RRID:AB_261041
Alexa Fluor 647 AffiniPure Donkey Anti- Goat	Jackson Immuno Research	Cat # 705-605-147; RRID:AB_2340437
Cy3 AffiniPure Donkey Anti - Rabbit	Jackson Immuno Research	Cat # 711-165-152; RRID:AB_2307443
Alex Fluor 488 AffiniPure Donkey Anti - Rat	Jackson Immuno Research	Cat # 712-545-153; RRID:AB_2340684
Cy3 AffiniPure Donkey Anti - Mouse	Jackson Immuno Research	Cat # 715-165-150; RRID:AB_2340813
Cy3 AffiniPure Donkey Anti - Rat	Jackson Immuno Research	Cat # 712-165-153; RRID: AB_2340667
Alex Fluor 488 AffiniPure Donkey Anti - Rabbit	Jackson Immuno Research	Cat # 711-545-152; RRID:AB_2313584
Donkey anti-Mouse IgG (H+L) Secondary Antibody, Alexa Fluor 488	Thermo Fisher Scientific	Cat # A-21202; RRID:AB_141607
Donkey anti-Rabbit IgG (H+L) Secondary Antibody, Alexa Fluor 488	Thermo Fisher Scientific	Cat # A-21206; RRID:AB_2535792
Donkey anti-Rabbit IgG (H+L) Secondary Antibody, Alexa Fluor 594	Jackson ImmunoReesearch	Cat # 711-585-152; RRID:AB_2340621
Donkey anti-Rat IgG (H+L) Secondary Antibody, Alexa Fluor 594	Thermo Fisher Scientific	CAT# A-21209; RRID:AB_2535795
Donkey anti-Rat IgG (H+L) Secondary Antibody, Alexa Fluor 488	Thermo Fisher Scientific	CAT# A-21208; RRID:AB_2535794
Donkey anti-Rat IgG (H+L) Secondary Antibody, Alexa Fluor 647	Jackson ImmunoReesearch	Cat # 712-605-153; RRID:AB_2340694
Donkey anti-Goat IgG (H+L) Secondary Antibody, Alexa Fluor Plus 647	Thermo Fisher Scientific	CAT# A32849; RRID:AB_2762840
Donkey anti-Goat IgG (H+L) Secondary Antibody, Alexa Fluor Plus Cy3	Jackson ImmunoReesearch	Cat # 705-165-147; RRID:AB_2307351
Mouse anti-spectrin alpha chain	Sigma Aldrich	CAT #MAB1622; RRID:AB_2307351
Mouse anti-phospho Tau	Cell Signaling	CAT #9632S; RRID:AB_2266237
Mouse anti-Tau	Cell Signaling	CAT #4019; RRID:AB_10695394
Anti-rabbit horseradish peroxidase-conjugated secondary antibody	Promega	CAT# W401B; RRID:AB_430833
Mouse monoclonal antibody for actin	Sigma Aldrich	CAT #A3854; RRID:AB_262011

(*Continued on next page*)

Continued

REAGENT or RESOURCE	SOURCE	IDENTIFIER
Bacterial and virus strains		
pAAV[TetOn]-TRE>ZsGreen1-rev(SYN1>tTS:T2A:rtTA)	Vector Builder	N/A
Chemicals, peptides, and recombinant proteins		
BrdU	Sigma-Aldrich	Cat # B5002; CAS:59-14-3
PBS	Sigma-Aldrich	Cat # P4417
0.1% Triton	Carl Roth	Cat # 3051
Bovine Serum Albumin	Sigma-Aldrich	Cat # A7906-100G
Fast green FCF stain	Sigma-Aldrich	Cat # 353-45-9
Low melting agarose	Biozym	Cat # 840101
Dako Mounting medium	Agilent	Cat # S3023
16% Formaldehyde Solution	Thermo Scientific	Cat # 28908
Normal Donkey Serum	Jackson Immuno Research	Cat # 017-000-121
Nuclease-free Water	Thermo Scientific	Cat # AM9937
Low TE buffer(10mM Tris - HCl pH 8.0, 0.1 mM EDTA)	Thermo Scientific	Cat # 12090-015
Ethanol	Millipore Sigma	Cat # E7023
10% Tween 20	Bio-Rad	Cat # 1662404
Glycerol	Ricca Chemical Company	Cat # 3290-32
DAPI (4',6-diamidine-2-phenylindole, dihydrochloride)	Invitrogen	Cat # D1306
RNase Zap decontamination solution	Invitrogen	CAT# AM9782
SPRIselect Reagent Kit	Beckman Coulter	Cat # B23318
Qiagen Buffer EB	Giagen	Cat # 19086
EBSS	Gibco	Cat # 24010043
Leibovitz's L-15 Medium	Gibco	Cat # 21083027
Platinum II Hot-Start Green PCR Master Mix	Thermo Scientific	Cat # 2907716
Critical commercial assays		
Papain Dissociation System	Worthington	Cat # LK003163
Chromium Single Cell Next GEM Single Cell 3' GEM kit v3.1	10x Genomics	PN-1000130
Library Construction Kit	10x Genomics	PN-1000196
Chromium Next GEM Single Cell 3′ Gel Bead Kit v3.1	10x Genomics	PN-1000129
Dual Index Kit TT Set A	10x Genomics	PN-1000215
RNeasy Lipid Tissue Mini Kit	Qiagen	CAT# 74804
Reverse Transcription Kit	Applied Biosystems	CAT# 4368814
Premix Ex Taq Probe based qPCR assay	Takara Biotechnology	CAT# RR390A
Invitrogen™ Click-iT™ EdU cell prolifetarion assay kit	Invitrogen	CAT# C10639
DNeasy Blood & Tissue Kit	Qiagen	CAT# 69504
Qubit™ 1X dsDNA Broad Range (BR) Assay Kit	ThermoFischer Scientific	CAT# Q33265
Deposited data		
scRNA-seq data	This study	GEO: GSE271794
Mass spectrometry data	This study	PXD047104
Experimental models: Organisms/strains		
Mouse-I4fA and B	Abad et al.[17]	N/A
Mouse-Nestin-Cre	Tronche et al.[85]	N/A

(*Continued on next page*)

Continued		
REAGENT or RESOURCE	SOURCE	IDENTIFIER
Mouse- B6.CgTg(APPSwFlLon,PSEN1* M146L*L286V)6799Vas/Mmjax	The Jackson Laboratory	RRID:MMRRC_034848-JAX
Mouse-B6.Cg-*Gt(ROSA) 26Sor*$^{tm1(rtTA,EGFP)Nagy}$	The Jackson Laboratory	RRID:IMSR_JAX:005670
Mouse- C57BL/6N	Charles River	RRID:MGI:2159965
Oligonucleotides		
See Table S4	N/A	N/A
Recombinant DNA		
Plasmid: FUW-tetO-hOKMS (this vector was modified to obtain FUW-tetO-EGFP-IRES-hOKMS).	Cacchiarelli et al., 2015[86]	Addgene plasmid #51543; RRID:Addgene_51543
pCAG-rtTA	Aihara et al., 2021[87]	Addgene plasmid # 163601; RRID:Addgene_ 163601
Software and algorithms		
ImageJ (Fiji), version 2.0.0-rc-69/1.53t	Schindelin et al., 2012[88]	https://imagej.net/Fiji
Rstudio	RStudio	https://www.rstudio.com/
LAS software	Leica Microsystems, Germany	http://www.leica-microsystems.com/products/microscope-software
Python, version 3.9.12	Python Software Foundation	https://www.python.org
CellProfiler, version 4.2.5	CellProfiler	http://cellprofiler.org
Imaris, version 9.5.1	Bitplane	https://imaris.oxinst.com/
Seurat, version 5.0.0	Rahul Satija lab	https://satijalab.org/seurat/
Cellranger, version 7.0.1	10x Genomics	https://www.10xgenomics.com/support/software/cell-ranger
GraphPad Prism, version 9/10	Domatics	https://www.graphpad.com/

EXPERIMENTAL MODELS AND STUDY PARTICIPANT DETAILS

Animals

Experiments were performed during development (from E10.5 till E17.5) or adult mice (>8 weeks). The wild-type animals were from the C57BL/6N strain (Charles River labs, https://www.criver.com/). We used the i4F-A mouse line described previously to perform all the crosses.[17] For developmental studies, i4F-Rosa refers to i4F-A carrying rtTA within the ubiquitously-expressed Rosa26locus.[17] I4F-Nes was developed by crossing both i4F-A and rtTA with the nervous system-specific Nestin-Cre.[85] This floxed rtTA transgenic line [B6.Cg-Gt(ROSA)26Sor<tm1(rtTA,EGFP)Nagy>/J] was imported from Jackson Laboratories (Stock# 005670).

In studies related to neurodegeneration, we utilized the previously described 5xFAD mouse line,[42] which was bred with the i4F-A mouse line. The animals were housed with access to food and water ad libitum in a colony room kept at 19°C–22°C and 40%–60% humidity, under a 12:12 h light/dark cycle. In all studies, Doxycycline (BioChemica) was administered in the drinking water supplemented with 7.5% of sucrose as previously described.[17]

Experimental animals were used in accordance with the ethical guidelines (Declaration of Helsinki and NIH Publication no. 85-23, revised 1985, European Community Guidelines, and approved by the UB (CEEA: 55/21) and regional government (Generalitat de Catalunya: 11559) ethical committees. Animal experiments conducted at the MPI were performed following regulations from the government of Upper Bavaria. The animal study was reviewed and approved by the Regierung von Oberbayern under the license 55.2-2532.Vet_02-20-49.

METHOD DETAILS

Experimental design using AAVs

We designed a viral construct to express rtTA only in principal neurons due to the AAV8 capsid and the Synapsin I promoter to drive the expression of the OSKM under the Tet-ON system. This pAAV8[TetOn]-TRE>ZsGreen1-rev(SYN1>tTS:T2A:rtTA virus was injected/transduced in the hippocampus of adult i-4F:WT and i-4F:5xFAD male mice at 8 weeks of age (see Figure 4A). At 12 weeks of age, all mice were treated with vehicle (VEH, sucrose 7.5%) or with doxycycline (Dox, 0.2 mg/kg in 7.5% sucrose) in drinking water 3 days/week. The treatment spanned 5 months. In the final month, when the mice were 8 months old, all were subjected to a comprehensive behavioral test battery (see Figure 7 and behavioral assessments down below for further details). Last day treatment, all mice were sacrificed for subsequent histological and Golgi studies.

Stereotaxic surgeries and viral constructs

Following anesthesia with ketamine/xylazine (100 and 10 mg/kg, respectively), we performed bilateral hippocampal injections of pAAV8[TetOn]-TRE>ZsGreen1-rev(SYN1>tTS:T2A:rtTA (2x1013 GC/ml in PBS, Vector Builder. Vector ID:VB210109-1009yyx). We used the following coordinates (millimeters) from bregma (anteroposterior and lateral) and from skull (dorsoventral); anteroposterior: −2.0; Lateral +/−1.25, and dorsoventral: −1.3 (CA1) and −2.1 (Dentate Gyrus). The cannula was left to deliver 1 μl of 1:1 virus in each depth during 2 min and five additional minutes were left to have complete virus diffusion. After 2 h of careful monitoring, mice were returned to their home cage for 4 weeks before starting the doxycycline (Dox) treatment.

Behavioural assessments

Plus Maze

To analyze mouse anxiety, we used the elevated plus maze paradigm. Briefly, the plus maze was made of plastic and consisted of two opposing 30 × 8 cm open arms, and two opposing 30 × 8 cm arms enclosed by 15-cm-high walls. The maze was raised 50 cm from the floor and lit by dim light. Each mouse was placed in the central square of the raised plus maze, facing an open arm, and its behavior was scored for 5 min. At the end of each trial, any defecation was removed, and the apparatus was wiped with 30% ethanol. We recorded the time spent in the open arms, which normally correlates with low levels of anxiety. Animals were tracked and recorded with SMART junior software (Panlab).

Novel Object Location Test (NOLT)

The novel object location memory task evaluates spatial memory and is based on the ability of mice to recognize when a familiar object has been relocated. Exploration took place in an open-top arena with quadrangular form (45 × 45 cm). The light intensity was 40 lux throughout the arena. Mice were first habituated to the arena in the absence of objects (1 d, 30 min). Some distal cues were placed throughout the procedure. On the second day during the acquisition phase, mice could explore two duplicate objects (A1 and A2), which were placed close to the far corners of the arena for 10 min. After a delay of 24 h, one object was placed in the diagonally opposite corner. Thus, both objects in the phase were equally familiar, but one was in a new location. The position of the new object was counterbalanced between mice. Animals were tracked and recorded with SMART Junior software (Panlab).

Cognitive flexibility and memory in a T-maze

The apparatus was a wooden maze consisting of three arms, two of them situated at 180° from each other and the third situated at 90° with respect to the other ones representing the stem arm of the T. All three arms were 45 cm long, 8 cm wide and enclosed by a 20 cm wall. The maze was thoroughly painted with waterproof gray paint. Light intensity was 10-20 lux throughout the maze. Two identical guillotine doors provided entry in the arms situated at 180°. In the training trial, one arm was closed (novel arm) and mice were placed in the stem arm of the T (home arm) and allowed to explore this arm and the other available arm (familiar arm) for 10 min, after which they were returned to the home cage. After inter-trial interval of 1 h mice were placed in the stem arm of the T-maze and allowed to freely explore all three arms for 5 min (testing phase). The first choice to turn either to the familiar arm or to the new arm (alternation rate, %) and the time spent in the two arms situated at 180° (time in the new arm*100/total time in the two arms at 180°) were the two parameters evaluated in the testing phase.

Y-maze spontaneous alternation

The spontaneous alternation performance was tested using a transparent symmetrical Y-maze. Five objects of similar size (∼20 cm3) and highly perceptible were situated surrounding the maze at ∼15–20 cm outside the walls. Each mouse was placed in the center of the Y-maze and could explore freely through the maze during an 8 min session. The sequence and total number of arms entered were recorded. Arm entry was complete when the hind paws of the mouse had been completely placed in the arm. Percentage alternation is the number of triads containing entries into all three arms divided by the maximum possible alternations (dividing the number of alternations by number of possible triads x 100). As the reentry into the same arm was not counted for analysis, the chance performance level in this task was 50% in the choice between the arm mice visited more recently (non-alternation) and the other arm visited less recently (alternation).

Forced Swimming Test

The forced swimming test was used to evaluate behavioral despair. Animals were subjected to a 6 min trial during which they were forced to swim in an acrylic glass cylinder (35 cm of height × 20 cm of diameter) filled with water, and from which they could not escape. The time that the test animal spent in the cylinder without making any movements beyond those required to keep its head above water was measured.

Passive Avoidance Test

For the passive avoidance (light-dark) paradigm, we conducted the experiments in a 2-compartment box, where 1 compartment was dimly lit (20 lux) and preferable to a rodent and the other compartment was brightly lit (200 lux); both chambers were connected by a door (5 cm × 5 cm). During training, mice were placed into the aversive brightly lit compartment; and upon the entry into the preferred dimly lit compartment (with all 4 paws inside the dark chamber), mice were exposed to a mild foot shock (2 s foot shock, 1 mA intensity). The latency of mice to enter into the dark chamber was recorded. Twenty seconds after receiving the foot shock, mice were returned to the home cage until testing. After 24 h (long-term associative memory), animals were tested for retention. In the retention test, mice were returned to the brightly lit compartment again, and the latency to enter the shock paired compartment (dark chamber) was measured (retention or recall latency). Ten minutes was used as a time cutoff in the retention test. The animals that learned the task would avoid the location previously paired with the aversive stimulus and showed a greater latency to enter it.

Accelerating rotarod

Animals were placed on a motorized rod (30-mm diameter, Panlab). The rotation speed was gradually increased from 4 to 40 r.p.m. over the course of 5 min. The fall latency time was recorded when the animal was unable to keep up with the increasing speed and fell. Rotarod training/testing was performed four times per day with 30 min as intertrial time interval. The results show the average of fall latencies per trial during the 2 days of training.

Marble test

Briefly, mice were individually placed in a clear plastic box (35 x 20 x 15 cm) filled with approximately 5 cm depth of wood chip bedding lightly pressed to give a flat surface. Twenty 1.5 cm diameter glass marbles were placed on the surface, evenly spaced, each about 4 cm apart, so to form 5 rows of 4. The completely unburied (OUT), partially unburied (>50% OUT), partially buried (>50% IN) and completely buried (IN) marbles were manually quantified at the end of a 20-min test session.

Three chamber social interaction test

The apparatus (40 x 40 x 60 cm) consisted of three interconnected lined compartments with open doors. Subject mice were habituated to the apparatus for 5 min. After the habituation phase, the subjects were tested in the sociability task for 10 min. An unfamiliar mouse (stranger) was placed in one of the side chambers enclosed in a small, round wire cage that allowed nose contact between the bars but prevented fighting. A second, empty round wire cage, was placed in the opposite compartment. The subject mouse had a choice between the first, unfamiliar mouse (stranger) and the empty wire cage (empty). Time exploring each small cage were measured using the SMART junior software (Panlab).

Golgi Staining and dendritic spine density analysis

Fresh brain right hemispheres were processed following the Golgi-Cox method as described previously.[89] Essentially, mouse brain hemispheres were incubated in the dark for 21 days in filtered dye solution (10 g L−1 K2Cr2O7, 10 g L−1 HgCl2, and 8 g L−1 K2CrO4). The tissue was then washed 3 × 2 min in water and 30 min in 90% ethanol (EtOH) (v/v); 200 μm sections were cut in 70% EtOH on a vibratome (Leica Microsystems) and washed in water for 5 min. Next, they were reduced in 16% (v/v) ammonia solution for 1 h before washing in water for 2 min and fixation in 10 g l−1 Na2S2O3 for 7 min. After a 2 min final wash in water, sections were mounted on superfrost coverslips, dehydrated for 3 min in 50%, then 70%, 80%, and 100% EtOH, incubated for 2 × 5 min in a 2:1 isopropanol:EtOH mixture, followed by 1 × 5 min in pure isopropanol and 2 × 5 min in xylol. Bright-field images of Golgi-impregnated stratum moleculare dendrites from hippocampal dentate gyrus granular neurons were captured with a Nikon DXM 1200F digital camera attached to a Nikon Eclipse E600 light microscope (100× oil objective). Only fully impregnated pyramidal neurons with their soma found entirely within the thickness of the section were used. Image z stacks were taken every 0.2 mm and at 1024 × 1024 pixel resolution, yielding an image with pixel dimensions of 49.25 × 49.25 mm. Z stacks were deconvolved using the Huygens software (Scientific Volume Imaging) to improve voxel resolution and to reduce optical aberration along the z axis. The total number of spines counting were performed by using the FIJI freeware (Wayne Rasband, NIH, RRID:SCR_003070)). At least 100-120 dendrites per group from at least 8-11 mice per group were counted. Picture acquisition and subsequent analysis were performed independently by two investigators blind to genotypes and results were then pooled.

Immunohistochemistry

Adult samples

Mice were euthanized by cervical dislocation. Left hemispheres were removed and fixed for 72 h in 4% paraformaldehyde (PFA) in PBS. Thirty-micrometer coronal sections were obtained using a Leica vibratome (Leica VT1000S) and then cryoprotected until use. Serial coronal sections were then washed three times in PBS, permeabilized 15 min by shaking at room temperature with PBS containing (v/v) 0.3% Triton X-100 and 3% normal goat serum (Pierce Biotechnology). After three washes, brain sections were incubated overnight by shaking at 4°C with antibodies for anti-Aβ (Mouse 1:500, 218111, clone NT78, Synaptic Systems. RRID:AB_11041707), anti-NeuN (Mouse 1:1000, MAB377, Chemicon. RRID:AB_2298772) and anti-Pyk2 (Rabbit, 1:500, P3902. Sigma. RRID:AB_261041), anti-Sirt1 (1:100, Cell Signaling, #2028. RRID:AB_1196631), anti-GFAP (1:500, DAKO, #z0334.), anti-Iba1 (1:500, Abcam, #Ab5076. RRID:AB_2224402), and anti-APP (Novus Biologicals, #NBP2-62566. RRID:AB_2917960) in PBS with 0.2 g/L sodium azide. After incubation with primary antibody, sections were washed three times and then placed 2 h on a shaking incubator at room temperature with the subtype-specific fluorescent secondary AlexaFluor-488 anti-rabbit (1:250, Thermo Fisher Scientific catalog #A32731, RRID:AB_2633280) or anti-mouse 555 (1:250, Thermo Fisher Scientific catalog #A32727, RRID:AB_2633276). No signal was detected in control sections incubated in the absence of the primary antibody. Images were acquired using a Zeiss LSM880 confocal laser scanning microscope or SP8 laser scanning confocal spectral microscope (Leica Microsystems, Germany). Images were taken using a 20× numerical aperture objective and 2 Airy disk pinhole and processed with ImageJ[90] (v1.53f) or Cell Profiler[91] (v.2) software. To characterize hippocampal astroglia and microglia, the entire 3D stack of images was obtained using the Z drive and analyzed using ImageJ. Microglia and astrocytes were automatically defined using the Li dark mask and selected with the wand tracing tool. Shape descriptors embedded in the software were applied as previously described.[92] For Aβ plaque analysis, images were captured using a Leica confocal SP5 with an x40 oil objective. The analysis involved manually counting Iba1-positive nuclei in contact with Aβ plaques and delineating the plaque's region of interest (ROI) to calculate the mean Iba1 intensity in the corresponding channel

Embryonic samples

Embryonic brains were fixed in 4% PFA over-night. Vibratome sections (50-70um thick) were incubated with primary antibodies after 2 hour of permeabilization and blocking with 1% BSA, 0.3% Triton X-100/PBS, 5% donkey serum (Pierce Biotechnology). We used

rabbit anti-Satb2 antibody 1/300 (Abcam), rat anti-Ctip2 1/300 (Abcam), rabbit anti-Pax6 1/300 (BioLegend), goat anti-Sox2 1/300 (R&D), rabbit anti-Histone H3 1/300 (Abcam), mouse anti-Pvim 1/300 (Abcam), rabbit anti-Oct3/4 1/300 (Bd Biosciences), rabbit anti-nanog 1/300 (Novus Biologicals) and mouse anti-Myc 1/300 (Santa Cruz). The secondary antibodies were Alexa Fluor 488-, 555- and 647-conjugated goat or donkey anti-rabbit/mouse/goat/rat (Molecular Probes 1:400). Images were acquired using a Zeiss LSM880 confocal laser scanning microscope or SP8 laser scanning confocal spectral microscope (Leica Microsystems, Germany). Images were taken using a 20× numerical aperture objective and 2 Airy disk pinhole and processed with ImageJ[90] (v1.53f) or Cell Profiler[91] (v.2) software.

Electron microscope experiments

As we previously described,[81] mice were transcardially perfused with a solution containing 4% PFA and 0.1% glutaraldehyde made up of 0.1 m PB, pH 7.4. Brains were then immersed in the same fixative for 12 h at 4°C. Tissue blocks containing the hippocampus were dissected and washed in 0.1 m PB, cryoprotected in 100 and 200 g/L sucrose in 0.1 m PB, and freeze-thawed in isopentane and liquid nitrogen. Samples were postfixed in 2.5% glutaraldehyde made up of 0.1 m phosphate buffer for 20 min, washed and treated with 2% osmium tetroxide in PB for 20 min. They were dehydrated in a series of ethanol and flat embedded in epoxy resin (EPON 812 Polysciences). After polymerization, blocks from the dentate gyrus (DG) region were cut at 70 nm thickness using an ultramicrotome (Ultracut E Leica Microsystems). Sections were cut with a diamond knife, picked up on formvar-coated 200 mesh nickel grids. For etching resin and remove osmium, sections were treated with saturated aqueous sodium periodate (NaIO4). They were then observed with a CM-100 electron microscope (Philips). Digital images were obtained with a CCD camera (Gatan Orius). In ultrathin sections, the density of synaptic vesicles in the molecular layer was calculated by counting the number of vesicles within a defined presynaptic area. The area of postsynaptic densities located in the molecular layer was also evaluated. All these calculations were performed using the ImageJ.

Mass spectrometry experiments

Fresh E15.5 mouse cortices or dentate gyrus from adult mice were homogenized for 1min at 4°C with an electric homogenizer using the following lysis buffer: 50 mM Tris-HCL (pH 7.4), 150mM NaCl, 2mM EDTA, 1% Triton X-100 and protease inhibitors (Roche ref. 04693116001). Samples were incubated on ice for 20 min and centrifuged for 10 min at 3000 rpm. Supernatant was collected and protein was measured using the Bio-Rad protein assay (Biorad, 5000001). 25-50 μl of protein at a final concentration of 1-2 μg/μl in lysis buffer were processed for mass spectrometry (MaxQuant run, Proteomic facility, Max Planck Institute of Biochemistry, Martinsried, Germany). 4-6 independent samples per processed per condition in all experiments. Analysis of differentially expressed proteins and volcano plots were generated using the DEP package in R-studio.

Cleared whole-mount embryonic brain

Dissected embryonic mouse brains were cleared by combining the protocols CUBIC[93] and RIMS.[94] Briefly, brains were fixed in 4% PFA overnight. After washing with PBS, they were immersed in CUBIC solution (25% Urea and 25% tetrakis in water) with gentle shaking till transparency at 37°. Brains were washed in PBS for 2d and post-fixed in 4% PFA for 2h. They were then stained with 5mM propidium iodine dissolved in PBS for 2d. Following another 1d PBS wash, samples were mounted in RIMS (76% Histodenz-0.02M PB-0.01%SodiumAzide-0.1%Tween-20) for confocal acquisition. Images were acquired using a Zeiss LSM880 confocal laser scanning microscope using a 10× numerical aperture objective and 2.5 Airy disk pinhole and processed with Imaris and ImageJ software.

Single-cell dissociation and Single-cell RNA-seq

Mouse brains at E15.5 were collected and sectioned under a vibratome (Leica VT1000S, Germany) in ice-cold Leibowitz medium with 5% FBS. The rostal region of cortex were collected using a scalpel. The tissue was subsequently dissociated into a single cell suspension with Worthington Kit and manually Papain dissociation system according to the recommended protocol (Worthington, #LK003163). A cell suspension of 2 CTR and 2 i4F-Nes samples were prepared for scRNA-seq. cDNA amplification and library construction were conducted with Chromium Single Cell Next GEM Single Cell 3' GEM kit v3.1 (PN-1000130), Library Construction Kit (PN-1000196), Chromium Next GEM Single Cell 3′ Gel Bead Kit v3.1 (PN-1000129) and Dual Index Kit TT Set A (PN-1000215) according to the manufacturer's instructions in the Chromium Single Cell 3′ Reagents Kits v3.1 User Guide. Transcriptome and barcode libraries were sequenced on NovaSeq 6000 at the Next Generation Sequencing Facility of the Max Planck Institute of Biochemistry.

Single-cell RNA-seq data processing

Barcode filtering and sequence alignment were performed using the CellRanger (v. 7.0.1) pipeline (http://10xgenomics.com). Reads were aligned to the mouse reference genome (10x genomics reference build MM10 2020 A). The gene-by-cell count matrices were further analyzed using Seurat R package (version 5.0.0) as follows: Cells from CTR and i4F-Nes samples were merged and filtered to retain only higher-quality cells (mitochondrial reads < 10%). Moreover, only genes expressed in at least 3 single cells were included for further analysis. Next, we normalized the data (normalization.method = 'LogNormalize', scale.factor = 10000), detected variable features (selection.method = 'vst', nfeatures = 3000), scaled the data (vars.to.regress = c('nCount_RNA')) and conducted principal component analysis (PCA). We retained 30 principal components for following nearest-neighbor graph construction and UMAP dimension reduction, and unsupervised clustering was conducted at a resolution of 0.8. We used Seurat's function

cc.genes.updated.2019 to obtain a list of genes associated with cell cycle, and the function CellCycleScoring to assign a cell cycle phase to each cell.

DNA methylation Clock

DNA was obtained from mice dentate gyrus. After homogenizing the tissue in 50 mM Tris-HCL (pH 7.4), 150mM NaCl, 2mM EDTA, 1% Triton X-100 and protease inhibitors (Roche ref. 04693116001), cell lysates were centrifuged for 10 minutes at 3000 rpm. Pellets containing the nuclei were processed for DNA isolation using the DNeasy Blood and Tissue kit according to the manufacturer's instructions (Qiagen, Hilden, Germany). Concentration of DNA samples was measured using the Qubit dsDNA BR kit (Invitrogen, Waltham, MA). DNA methylation epigenetic age was assessed using DNA methylation data obtained on the Horvath mammal 320k array[48]. Raw methylation array data was normalized using SeSAMe (Zhou et al. 2018[95]) and epigenetic clocks were computed using the guidelines and source code by the Mammalian Methylation Consortium.
(https://github.com/shorvath/MammalianMethylationConsortium/).

In utero electroporation

In utero electroporation was performed at E13.5 on anesthetized C57BL/6 mice using standard procedures. DNA plasmids were used at 1 μg/μl (FUW-tetO-EGFP-IRES-hOKMS or FUW-tetO-EGFP with pCAG-rtTA) and mixed with 1% fast green (Sigma-Aldrich, final concentration 0.2%). Plasmids were injected into the ventricle with a pump-controlled micropipette. After injection, six 50 ms electric pulses were generated with electrodes confronting the uterus above the ventricle. The abdominal wall and skin were sewed, and the mice were kept until E16.5 embryonic stage treated with 0.2mg/ml of Dox in the drinking water.

Western blot

Animals (n=4–6 per group) were sacrificed by cervical dislocation. The hippocampus was dissected out, frozen using CO2 pellets, and stored at -80°C until use. Briefly, the tissue was lysed by sonication in 250 μl of lysis buffer as described elsewhere. Supernatant proteins (15 ug) from the dentate gyrus extracts were loaded in SDS–PAGE and transferred to nitrocellulose membranes (GE Healthcare, LC, UK). Membranes were blocked in TBS-T (150 mM NaCl, 20 mM Tris- HCl, pH 7.5, 0.5 ml Tween 20) with 5% BSA and 5% non-fat dry milk. Immunoblots were incubated overnight at 4º with anti-spectrin alpha chain (Sigma Aldrich, #MAB1622) at 1:1000, anti-phospho Tau (Cell Signaling, #9632S) at 1:1000, anti-Tau (Cell Signaling, #4019S) at 1:1000, anti-GFAP (DAKO, #z0334) at 1:100, anti-H3K9me3 (Cell signaling, #9646) at 1:300 in PBS with 0.2% Sodium Azide. After three washes in TBS-T, blots were incubated for 1 h at room temperature with anti-rabbit horseradish peroxidase-conjugated secondary antibody (1:2000; Promega, Madison, WI, USA) and washed again with TBS-T. Immunoreactive bands were visualized using the Western Blotting Luminol Reagent (Santa Cruz Biotechnology) and quantified by a computer-assisted densitometer (Gel-Pro Analyzer, version 4, Media Cybernetics). For loading control, a mouse monoclonal antibody for actin was used (1:100.000, Sigma Aldrich, #A3854).

EdU and BrdU

Pregnant mice were injected with BrdU or EdU (50μg/g) either 3 days or 30 minutes before sacrifice. Embryonic brains were fixed with 4% PFA overnight and cut in 70μm sections with vibratome. Edu was revealed following instructions of Click-iT EdU cell proliferation assays kit: Sections were incubated for 30 minutes on 3% BSA then another 30 minutes on Click-iT® EdU reaction cocktail (440μL 1X Click-iT® reaction buffer + 10 μL Copper protectant + 1.2 μL Alexa Fluor® picolyl azide (Component B) + 50 μL 1X Click-iT® EdU buffer additive) and then washed with 3% BSA. For BrdU staining, sections were pretreated with 2N HCl for 30 min and subsequently neutralized with sodium-tetraborate (Na2B4O7 0.1M, pH: 8.5) for 2 × 15 min. Staining was performed using mouse anti-BrdU (Roche) antibody.

RNA isolation and RT-qPCR

RNA extraction from mice brain samples was extracted by RNeasy Lipid Tissue Mini Kit (cat. No. 74804) manufacturer's instructions. The purified RNA was eluted in 30 μL of nuclease-free H2O and the quantification was measured using a ND-1000 spectrophotometer (Thermo Fisher Scientific). Samples were stored at -80°C until use. cDNA synthesis and analysis of gene expression by Real-time quantitative PCR (qPCR) assay. The High Capacity cDNA Reverse Transcription Kit (Applied Biosystems, ref. 4368814) was used to reverse transcribe 500 ng of total RNA by the manufacturer's instructions. To evaluate housekeeping and interest genes, Integrated DNA Technologies (IDT) provided PrimeTime qPCR Assays (Table S4). The qPCR reaction was carried out using the Premix Ex Taq Probe based qPCR assay (Takara Biotechnology, ref. RR390A) on 96-well plates with a final volume of 12 μL. StepOnePlus Real-Time PCR System (Applied Biosystems) was used to conduct each reaction in triplicate set to the following program: 1 cycle 95 °C for 30 seconds; 40 cycles at 95 °C for 5 seconds and 60 °C for 20 seconds.

QUANTIFICATION AND STATISTICAL ANALYSIS

Statistical analyses were performed using GraphPad Prism v.8 (GraphPad Software, La Jolla, California, USA). A two-tailed unpaired Student's t-test was employed when comparing two groups, while one-way ANOVA with Tukey's post hoc analysis or two-way

ANOVA with Bonferroni's post hoc test was used for multiple group comparisons, as appropriate. Normal distribution was tested with d'Agostino and Pearson omnibus test. In case of no normal distribution corrections were applied Mann-Whitney or Dunn's test. Cell cycle distribution statistics between CTR and i4F-Nes was calculated with X-squared analysis.P values represent *$p \leq 0.05$, **$p \leq 0.01$, ***$p \leq 0.001$ and ****$p \leq 0.0001$. All data are presented as the mean ± s.e.m, whisker plots or dot plots. Circles indicate values of individual mice or cells (Figure 1E). All sample sizes and definitions are provided in the figure legends. All experiments in this study were conducted in a blinded and randomized manner. All mice bred for the experiments were used for preplanned experiments and randomized to experimental groups.